Automated Detection and Depth Determination of Melt Ponds on Sea Ice in ICESat-2 ATLAS Data — The Density-Dimension Algorithm for Bifurcating Sea-Ice Reflectors (DDA-bifurcate-seaice)

Ute Herzfeld, Thomas Trantow, Huilin Han, Ellen Buckley, Sinéad Farrell, Matthew Lawson

***Abstract*—As climate warms and the transition from a perennial to a seasonal Arctic sea-ice cover is imminent, understanding melt ponding is central to understanding changes in the new Arctic. NASA's Ice, Cloud and land Elevation Satellite (ICESat-2) has the capacity to provide measurements and monitoring of the onset of melt in the Arctic and on melt progression. Yet ponds are currently not reported on the ICESat-2 standard sea-ice products because of the low resolution of the products, in which only a single surface is determined.**

The objective of this paper is to introduce a mathematical algorithm that facilitates automated detection of melt ponds in ICESat-2 ATLAS data, retrieval of two surface heights, pond surface and bottom, and measurements of depth and width of melt ponds. With the Advanced Topographic Laser Altimeter System (ATLAS), ICESat-2 carries the first space-borne multi-beam micro-pulse photon-counting laser altimeter system, operating at 532 nm frequency. ATLAS data are recorded as clouds of discrete photon points. The Density-Dimension Algorithm for bifurcating sea-ice reflectors (DDA-bifurcate-seaice) is an auto-adaptive algorithm that solves the problem of pond detection near the 0.7m nominal alongtrack resolution of ATLAS data, utilizing the radial basis function for calculation of a density field and a threshold function that automatically adapts to changes in background, apparent surface reflectance and some instrument effects. The DDA-bifurcate-seaice is applied to large ICESat-2 data sets from the 2019 and 2020 melt seasons in the multi-year Arctic sea-ice region. Results are evaluated by comparison to those from a manually forced algorithm.

***Index Terms*—satellite altimetry, cryospheric sciences, computational algorithm, melt pond, arctic sea ice, ICESat-2.**

I. Introduction

As the Arctic sea ice has been reported to reach historic lows repeatedly [Stroeve et al., 2007], [Stroeve et al., 2012], [Serreze et al., 2007], [Serreze et al., 2008], [Stroeve and Notz, 2018], [Petty et al., 2018] and transition from a perennial to a seasonal Arctic sea-ice cover is imminent [Kwok, 2018], [Stroeve and Notz, 2018], melt ponding is a key process. [Perovich et al., 2003] alert to the complexity of melt ponds and their evolution on the thinning sea ice. Predictions based on models diverge [Stroeve et al., 2007], [Scott and Feltham, 2010], [Kay et al., 2011], [Jahn et al., 2011], [Hunke et al., 2013], [Notz and Community, 2020]. Since any predictions are only as good as the data they are based on, satellite observations are essential in understanding changes in the Arctic cryosphere and constraining models. NASA's Ice, Cloud and land Elevation Satellite (ICESat-2), launched September 15, 2018, has the capacity to provide measurements and monitoring of the onset of melt in the Arctic and on melt progression [Farrell et al., 2020], [Buckley et al., 2020b], [Tilling et al., 2020]. Yet, ponds are generally missed in the standard data product ATL07, because of the low resolution of the product [Kwok et al., 2021a], [Kwok et al., 2021c]. ATL07 reports only a single surface height, and in some cases, this height is determined as somewhere between the height of the surface and that of the melt-pond bottom [Farrell et al., 2020]. Missing ponds or confusing ponds with sea-ice leads can result in miscalculation of freeboard, which is reported in ICESat-2 data product ATL10 [Kwok et al., 2021b], see [Farrell et al., 2020].

What appears to be a discrepancy between the observation capabilities of the sensor and the current status of official data products can be explained by a combination of the spatial scale of change signals in Arctic sea ice and mathematical algorithms applied in data analysis. The sea-ice ICESat-2 ATLAS data products ATL07 and ATL10 [Kwok et al., 2021c], [Kwok et al., 2021b] have facilitated significant findings on sea-ice freeboard and seasonal changes for the entire Arctic and Antarctic sea-ice regions [Kwok et al., 2019b], [Kwok et al., 2019c], [Kwok et al., 2019a]. With the Advanced Topographic Laser Altimeter System (ATLAS), ICESat-2 carries the first space-borne multi-beam micro-pulse photon-counting laser altimeter system. ATLAS registers returns from every photon in the 532 nm (green light) spectral band of the sensor, including photons from ambient light (background photons) in addition to signal photons, which together form a photon point cloud, reported on the product ATL03 [Neumann et al., 2019], [Neumann et al., 2021a], [Neumann et al., 2021b]. The mathematical algorithms applied to derive the ICESat-2 ATLAS Sea-Ice Products [Kwok et al., 2021a] yield information per

Manuscript received September 30, 2022.

This work was supported by the U.S. National Aeronautics and Space Administration (NASA) Earth Sciences Division under awards 80NSSC20K0975, 80NSSC22K1155, 80NSSC18K1439 and NNX17AG75G (Principal Investigator Ute Herzfeld) and 80NSSC20K0966 and 80NSSC17K0006 (Principal Investigator Sinead Farrell).

Ute C. Herzfeld, Thomas Trantow, Huilin Han and Matthew Lawson are with Geomathematics, Remote Sensing and Cryospheric Sciences Laboratory, Department of Electrical, Computer, and Energy Engineering, University of Colorado Boulder, Boulder, CO 80309 U.S.A. (email: ute.herzfeld@colorado.edu).

Sinéad Farrell and Ellen Buckley are with Departments of Geographical Sciences and Atmospheric & Oceanic Science, University of Maryland, College Park, MD, 20742, U.S.A.

along-track segment area, whose length depends on fixed 150 photon counts and thus is variable, typically between 17 m by 27 m and 17 m by 200 m, while the ATLAS sensor results in a nominal along-track spacing of 0.7 m (under clear-sky atmospheric conditions). This spatial resolution is sufficient for documentation and analysis of changes in the entire Arctic or Antarctic regions, but not for detection of melt ponds.

Analyses of ATL03 data collected over Arctic sea ice show that melt ponds, snow depth, ridged and rubbled ice are resolved in the photon cloud, which suggests that geophysical processes can be studied that lead to the formation of these high-resolution signatures in the ice [Farrell et al., 2020], [Buckley et al., 2020b], [Tilling et al., 2020]. To automatically detect and report melt ponds in ICESat-2 ATLAS data and measure their depth, a new algorithm needs to be developed that builds on the ATL03 photon cloud. In this paper, we introduce such an algorithm.

More formally, a high-resolution algorithm that facilitates retrieval of two surfaces wherever such exist is required to report melt pond existence and depth from ICESat-2 data. In order to allow operational application for ICESat-2 photon data across large and small regions alike (including the entire Arctic and Antarctic sea-ice regions), such a melt-pond algorithm needs to meet the following criteria:

1) The algorithm needs to be fully automated (i.e. it should not require a-priori information on the existence or location of a pond)
2) detect ponds wherever they exist
3) avoid false positives
4) automatically adapt to different background characteristics of daytime and nighttime data and to changes in apparent surface reflectance (ASR)
5) find ponds among sea-ice of different roughness types (smooth, ridged, and complex)
6) correctly determine the start and end points of a pond along the ICESat-2 ground track
7) measure the pond depth
8) represent the complexity of the sea-ice at high resolution.

In this paper, we introduce an algorithm for melt-pond detection from ICESat-2 data that satisfies the above criteria, building on our concept of the Density-Dimension Algorithm (DDA) for ICESat-2 data analysis [Herzfeld et al., 2017], [Herzfeld et al., 2021c], [Herzfeld et al., 2021a], [Herzfeld et al., 2021b], which facilitates ice-surface height determination at the 0.7 m nominal resolution of the sensor. The new sea-ice algorithm is termed Density-Dimension Algorithm for bifurcating sea-ice reflectors (DDA-bifurcate-seaice or DDA-bif-seaice for short).

The complexity of the task of automated melt-pond detection and depth measurement is illustrated in [Perovich et al., 2003] (fig. 3 and fig. 11), who collected mass-balance measurements during the Surface Heat Budget of the Arctic Ocean (SHEBA) experiment conducted October 1997-October 1998. A simple algorithm for depth measurement of ponds has been described and applied in [Farrell et al., 2020], [Buckley et al., 2020a], [Buckley et al., 2019] (UMD-melt-pond-algorithm (MPA)). Their algorithm requires knowledge where a pond exists, it is not automated and thus cannot be employed for operational processing of ICESat-2 products.

This paper will include a mathematical description of the DDA-bif-seaice and application to ICESat-2 data from the Lincoln Sea. The DDA-bif-seaice will be applied to analyze ICESat-2 ATLAS data from melt-pond regions in the Lincoln Sea and other parts of the multi-year ice regions of the Arctic Ocean.

As a means of evaluation, results from the DDA-bif-seaice will be compared to results from a simple algorithm for analysis of melt ponds in ICESat-2 ATLAS that requires a-priori manual identification of ponds, developed at the University of Maryland (UMD Melt-Pond Algorithm (MPA)). The UMD MPA, described in [Buckley, 2022], [Buckley et al., prep], is not automated and thus cannot be employed for operational processing of ICESat-2 products.

The DDA-bif-seaice is applied in a large-scale analysis of ICESat-2 ATLAS data sets to study melt onset and the evolution of melt ponds on multi-year sea-ice in the Arctic, reported in a companion paper [Buckley et al., prep] that also uses the UMD MPA.

II. ICESat-2 in a Nutshell

A. Main Characteristics of Instrumentation, Observation and Resultant Data

ICESat-2 ATLAS is a micro-pulse photon-counting laser altimeter system, which collects data in three pairs of two beams, a strong beam and a weak beam, where the energy of the weak beam is a quarter of that of the strong beam [Markus et al., 2017], [Neumann et al., 2019]. Across-track separation of the beams on the Earth's surface is 3.3 km between the centers of adjacent pairs and 90 m for the beams within each pair; ICESat-2 beam pattern and track geometry are illustrated in [Herzfeld et al., 2021c] (Fig. 3). The sensor operates in the 532 nm wavelength (green light) with a pulse-repetition rate (PRF) of 10 kHz. The PRF results in a nominal 0.7 m spacing of the laser pulses on the Earth's surface, under clear-sky atmospheric conditions. ATLAS has a footprint diameter of less than 17.4 m at 85% encircled energy. The Field of View (FOV) of the receiver telescope is 83.8 μrad, equivalent to 45 m FOV on the surface of the Earth. Observatory performance has been assessed in [Magruder et al., 2021], where the actual footprint is characterized as closer to 10 m in diameter. As the FOV moves along the satellite ground track and returns from every single photon (in the 532 nm wavelength domain of the sensor) are recorded, surface structures at much higher resolution than footprint diameter can be resolved (see sections (2.2) and [Herzfeld et al., 2021c]). The instrumentation and derivation of the recorded photon point cloud are described in [Neumann et al., 2019], and any technical component of the instrument and data set necessary for understanding the work in this paper is found in [Herzfeld et al., 2021c]. Information in this section is modified after [Herzfeld et al., 2022], where a validation of the ICESat-2 data collection over complex land ice surfaces is performed.

The ATLAS system records returns from every single photon in the 532 nm range of the sensor as a photon point cloud. In addition to the photons that result from the active lidar signal (signal photons), the photon point cloud also includes background photons that stem from ambient light in the 532 range of the spectrum and artefacts due to instrument effects such as dead-time effect and afterpulses. The identification of signal photons in the point cloud or classification of signal versus background photons constitutes an ill-posed mathematical problem.

B. Standard ICESat-2 ATLAS Sea-Ice Products: ATL07 and ATL10

The current standard data products for sea ice are ICESat-2 ATLAS products ATL07 Sea Ice Height [Kwok et al., 2021c] and ICESat-2 ATLAS ATL10 Sea Ice Freeboard [Kwok et al., 2021b]. The derivation of the standard sea-ice data products ATL07 and ATL10 is described in the Algorithm Theoretical Base Document (ATBD) for ATL07 and ATL10 [Kwok et al., 2021a]. The ATL07 algorithm is not based on a fixed spatial resolution, but rather on a fixed number of recorded photons, which results in sea-ice height determinations of variable size, typically on the order of 25 km. A Wiener Filter is employed as the core means of photon-data analysis. The ATL07 algorithm is aimed at resolving a single surface height. Thus, it does not resolve melt ponds. The determination of sea ice freeboard can also be affected by errors in the surface height determination [Farrell et al., 2020].

III. Overview of the Approach DDA-bif-seaice and Examples of Melt-Pond Detection

The central objective of this paper is to introduce the DDA-bifurcate-seaice and apply it to detection and depth determination of melt pond in Arctic sea ice. A first view of results of the DDA-bif-seaice is given in Fig. 1, which illustrates that ponds can be detected across a range of different environments indicated by different surface morphologies, as well as for the central and outer beams of the ATLAS instrument. The fact that ponds are found in situations of highly variable apparent surface reflectance, indicated by the colors of the signal photons in Fig. 1, points at the auto-adaptive capability of the algorithm.

Fig. 1a shows a large (over 200m diameter) melt pond that is located among ridged sea ice and has a complex bottom topography, Fig. 1b illustrates detection of shallow and relatively deep (3m) ponds among smooth and ridged ice. The right pond (at 335800) is located among fault blocks, in a location that is typical for formation of melt ponds and thus of interest for process studies. From the view point of a detection algorithm, the sequence of ponds in Fig. 1b illustrates a set of bifurcation points (points where one sea-ice surface splits into two surfaces of melt-pond top and melt-pond bottom) and rejoining points (where the two surfaces comes again together at the end of a melt pond). The set of bifurcation and rejoining points will be identified in the DDA-bif-seaice algorithm to facilitate identification of entire individual points, tracking of ponds across analysis steps and calculation of statistical values such as depth (range) and pond width (in the along-track direction). Ponds are identified in situations of weak surface reflectance (e.g. Fig. 1e, 1g, 1h), strong surface reflectance (Fig. 1b, 1c, 1f) with density values of 250, and mixed surface reflectance (Fig. 1a). The ICESat-2 observatory yields observations through a complex geometry, illustrated in [Herzfeld et al., 2021c] (Fig. 3) and (Table 1), the strong beam in a pair of beams can be either the right beam or the left beam (e.g. gt2r or gt2l), depending on whether ATLAS flies forward or backward (orientation changes every few months). Ponds can be identified in the outer beams, for example, in gt3l in Fig 1a, 1d, 1e, 1f and in gt1l in Fig. 1b, 1c, as well as in the center beam, gt2l, in Fig. 1g, 1h. All examples in Fig. 1 stem from strong beams, but ponds are also detected in data from the weak beam.

The examples may also serve to provide a first understanding of the tasks that the DDA-bif-seaice performs and as such motivate the mathematical description of the algorithm, given in section 4.

Following the mathematical description, the DDA-bif-seaice will be applied to data from the multi-year Arctic sea-ice region, for two different years, 2019 and 2020, during melt season (Section 5). Corrections for speed of light in sea water to calculate depth from range and challenges for the algorithm are discussed in section 5 as well. Results from the DDA-bif-seaice will be compared to results reported on ICESat-2 standard product ATL07 to demonstrate the increase in information content.

IV. Algorithm: The DDA-bifurcate-seaice

A. The Family of Density-Dimension Algorithms

The Density-Dimension Algorithm for bifurcating reflectors (DDA-bif) is part of the density-dimension algorithm family. The density-dimension algorithms have been developed for the analysis of micro-pulse photon-counting lidar altimeter data, especially data collected with the ICESat-2 ATLAS instrument and its airborne predecessors such as the SIGMA, MABEL and SIMPL instruments, and include algorithms for ice surface data (the DDA-ice) [Herzfeld et al., 2017], [Herzfeld et al., 2021c], [Herzfeld et al., 2022], for vegetation data (the DDA-sigma-veg) [Herzfeld et al., 2014] and for atmospheric layers (the DDA-atmos) [Herzfeld et al., 2021a], [Herzfeld et al., 2021b]. Common to all density-dimension algorithms is the ability to retrieve surfaces and other reflectors in situations of complex spatial data distributions and mathematically difficult signal-to-noise relationships. Examples include crevassed and otherwise morphologically complex ice surfaces, vegetation canopy and ground under canopy, and tenuous atmospheric layers such as optically thin clouds, blowing snow and aerosol layers. The DDA-atmos is the algorithm applied for identification of atmospheric layers and surface in the ICESat-2 atmospheric data product, ATL09 (see also, [Palm et al., 2021]).

B. DDA-ice Mathematical Philosophy

The DDA-bif-seaice builds on the density-dimension algorithm for ice surfaces (DDA-ice or DDA-ice-1). The DDA-ice is the original algorithm for ice surfaces and the name

DDA-ice-1 indicates that it follows a single surface (more technically, the DDA-ice-1 performs a single density run).

The main idea of the DDA-ice is that signal photons are expected to have a neighborhood with a larger photon density than background photons. To quantify density, photons are aggregated using a Gaussian *rbf*. A *rbf* is a real-valued function whose value decreases with distance from the center c:

$$\Phi(x, c) = \Phi(\|x - c\|) \tag{1}$$

for all x in a definition area $\mathcal{D}$ with respect to any norm $\|\cdot\|$. The density field of the photon cloud is calculated by letting each single photon take the role of a center, evaluating the *rbf* for all neighboring photons and forming the sum of weights from this process [Herzfeld et al., 2017]. Density is considered a dimension of the data set and signal-background separation is performed by an auto-adaptive threshold function in the geolocation-density domain. The auto-adaptive capability of the algorithm implies that a threshold function is used which automatically adapts to the variable background characteristics of day-time and night-time observations in the photon point cloud (a lot more photons from ambient light are recorded during day-time), Apparent Surface Reflectance (ASR) and other, including instrumental, sources of background photons. The results of the DDA-ice-1 are not disturbed by instrument-related background photons, such as those resultant from after-pulses (because these are less dense than the surface signal). Surface height among and between signal photons is determined using a ground-follower, a function that automatically adapts to surface roughness. The option for areas of high surface roughness, originally designed for surface-height determination over crevassed glaciers, facilitates surface-height determination of ridged and rubbled sea-ice, while the option for low surface roughness works well for simple, smooth surfaces of marine and terrestrial ice environments [Herzfeld et al., 2017], [Herzfeld et al., 2021c]. The DDA-ice-1 resolves surface heights at the resolution of the sensor, i.e. of the point-cloud data (nominally 0.7m along-track) and height segments of 5 m or 2.5 m, depending on surface roughness [Herzfeld et al., 2021c].

C. Input Data, Algorithm Development and Version

As input for analysis, the DDA-bifurcate-seaice uses the geolocated photon point cloud, which includes signal and background photons, as reported in the ICESat-2 ATLAS ATL03 data product [Neumann et al., 2021a], [Neumann et al., 2019], [Neumann et al., 2021b]. The DDA algorithms do not use the photon classification that is provided on ATL03 [Herzfeld et al., 2021c]. The ATL03 data sets are publicly available via the NASA Earthdata site and updated at regular time intervals of about 6 months.

Analyses in this paper utilize the ICESat-2 ATLAS data products ATL03 (ATLAS/ICESat-2 L2A Global Geolocated Photon Data), Version 5 [Neumann et al., 2021a], described in the Algorithm Theoretical Base Document for ATL03 [Neumann et al., 2021b].

The algorithm DDA-bif-seaice was developed on local desktops (iMacs) of the Geomathematics, Remote Sensing and Cryospheric Sciences Laboratory at the University of Colorado Boulder, the computational code is implemented using python 3. The algorithm described in this paper is that of DDA-ice geomath version v18.0 (latest version as of June 2022; committed December 2021).

For processing of large amounts of ICESat-2 ATLAS collected over the multiyear Arctic sea-ice region, the DDA-ice-bifurcate was transferred to the NASA cloud (ADAPT). Results are reported in the companion paper on evolution of melt ponding [Buckley et al., prep]. An advanced version of the DDA-bif-seaice algorithm may be included in a future version of the standard ICESat-2 products.

D. Challenges Specific to Melt-Pond Detection over Seaice

The occurrence of melt ponds is by no means specific to sea ice, as melt ponding occurs over glaciers, ice sheets and snow fields as well [Fricker et al., 2020]. There are, however, challenges specific to melt-pond detection over sea ice, which warrant the development of a specific sea-ice algorithm. We have developed an algorithm for bifurcating reflectors, aimed at detection of large melt ponds on Amery Ice Shelf and for detection of melt ponds and channels on the Greenland Ice sheet [Herzfeld et al., prep]. The ponds on land ice and ice shelves are much larger (kilometers to tens of kilometers) and deeper than those on sea ice, thus the identification of bifurcation and rejoining locations of the two surfaces, pond surface and pond bottom, is naturally much more robust to the selection of algorithm-specific parameters that determine the resolution, and false positives are avoided relatively easily. The situation for sea ice is much more complex. Ponds can form in smooth sea-ice regions as well as in ridged ice areas, where ponds typically occur on the side of a faulted sea-ice block. The ridge height is often larger than the pond depth, creating an additional challenge for an automated detection algorithm.

An additional challenge is due to the fact that sea-ice is, simplified, stratified into frozen seawater overlain by a snow layer and the two layers interact differently with the incoming lidar signal. The penetration, scattering and reflection properties of lidar signals in complex media are far from understood (see, for example, [Smith et al., 2018]) As melting progresses, snow and ice transforms into slush, forming sea-ice ponds in the making, which can already be seen in the lidar signal (for example, in Fig. 1d). Other examples illustrating the complexity of sea ice include ponds with a solidly frozen surface, where a pond formed and the surface refroze, subnivean ponds, ponds with solid bottoms (Fig. 1a) and ponds with ill-defined bottoms (Fig. 1c). For imagery of sea-ice as well as other remote-sensing observations, we refer to [Maslanik et al., 2006], [Sturm et al., 2006], [Herzfeld et al., 2006].

We have previously described a second-order algorithm, the DDA-ice-2, for the case that the stronger reflecting surface is always on top [Herzfeld and Trantow, prep]. For the melt-pond detection problem, this assumption cannot be made. The stronger reflecting surface can be the top of a melt pond or its bottom, or both surfaces can be of similar strength, or the strength of the reflector may even switch from top to bottom depending on location. These complexities of the problem motivate the development of a DDA-bifurcate for analysis of lidar data over sea ice.

A key challenge in designing a melt-pond-detection algorithm for photon-cloud data (such as ATL03 data) lies in identification of bifurcation locations of the reflecting surfaces and in identifications of locations where the two surfaces rejoin (rejoining locations). The bifurcation algorithm needs to be robust w.r.t. the distribution of the point-cloud data: (a) To identify small and shallow ponds, with the goal of vertical resolution of 0.1 m and (b) to avoid false positives (locations that show point clusters at two or more different heights, where a pond does not exist).

A problem that is especially severe in the analysis of sea-ice data is posed by the occurrence of signal saturation, which in combination with the detector dead-time effect leads to delayed registration of photon, resulting in apparent secondary layers below the actual surface at (pseudo-) depths that overlap with typical depths of melt ponds on sea ice. There are several such pseudo-depths, at 0.43 m and farther below. This problem is addressed in subsection (5.3).

E. Algorithm Steps of the DDA-ice-1

The DDA-bif-seaice builds on the DDA-ice-1 (there called the DDA-ice), the algorithm for primary surface detection, as described in [Herzfeld et al., 2017]. Here, we describe the algorithm to the extent necessary to understand the concept of the DDA-bif-seaice. the algorithm steps are illustrated in Fig. 2 for an example of ATLAS data over seaice. The algorithm is driven by a set of algorithm-specific parameters, described in [Herzfeld et al., 2017]. Parameters specific to the DDA-bif-seaice and the analysis described in this paper are given in Table 1.

The DDA-ice-1 has the following steps:

1) Large-scale separation of signal and noise slabs
2) Calculation of the density field using the radial basis function, *rbf*
3) Operation of an auto-adaptive threshold function to separate noise and signal photons, using density as an additional dimension.
4) Application of a piece-wise linear ground follower with 1-10m resolution over smooth surfaces and 0.5-5m over crevasses, sastrugi and other rough surfaces. The ground follower automatically adapts to surface roughness.

Step 1. Separation of signal and noise slabs. The large-scale separation of signal and noise slabs utilizes a simple histogram-based criterion that evaluates photon counts. The signal slab centers in height around the height bin of strongest return (highest photon count) and the noise slab is determined as the slab of same height interval located immediately above the signal slab. For sea ice, the slab thickness is 30 m.

Step 2 Calculation of the density field. The density field is calculated for every single photon, using that photon as the center point, c of a kernel. A Gaussian *rbf*, formally defined in eqn. 1, is evaluated as follows, letting $r = x - c$ and $s \in \mathcal{R}$:

$$\Phi(r) = \frac{1}{\sqrt{2\pi s^2}} e^{-(\frac{r}{\sqrt{2}s})^2} \tag{2}$$

For each point in the definition set $\mathcal{D}$ (each photon in the cloud, for both signal and noise slabs), a density value $f_d(c)$ is calculated as:

$$f_d(c) = \sum_{x \in \mathcal{D}_c} W_c(x) \tag{3}$$

for all x within the search region $\mathcal{D}_c$, where the weights $W_c(\cdot)$ are derived from the *rbf* (see eqn. 11 in [Herzfeld et al., 2017]). The kernel can be visualized as a Gaussian bell curve rotated around the x-axis.

Algorithm-specific parameters. The kernel of the *rbf* is controlled by the algorithm-specific parameters standard deviation σ, anisotropy a and cutoff κ, where κ is the number of standard deviations used to define the extent of the search region. For $a \neq 1$, points with the same *rbf* value $\Phi(\|x - c\|_a)$ are located on an ellipsoid with axes (a,a,1) around the center point c, rather than on a circle. In the original density-dimension algorithm, anisotropy is selected such that the resultant ellipsoid has a longer axis parallel to the horizontal, motivated by the idea that the probability of finding more ground signal points is larger in the approximately horizontal direction than in the vertical direction; for a validation of this concept and examples from the ICESat-2 airborne simulator, SIMPL, data see [Herzfeld et al., 2017]. The fact that typical sea ice has a large horizontal extension motivates the use of a large anisotropy fact of $a = 20$.

With anisotropy, the density value, $f_{d,a}(c)$, is calculated as

$$f_{d,a}(c) = \sum_{x \in \mathcal{D}_{c,a}} W_{c,a}(x) \tag{4}$$

This calculation is carried out for each photon as a center point and yields the density field.

Step 3. Threshold function. An auto-adaptive threshold function, described in [Herzfeld et al., 2017], is employed to separate signal and noise photons. The threshold function is controlled by a quantile and threshold-offest as algorithm-specific parameters (see, Table 1).

In this algorithm version (DDA-ice-py3, v18.0) we use a two-step threshold function. In the first step, the maximum of density values of photons in the noise slab is calculated, and photons with a density value larger than this maximum plus a threshold-offset value are passed into a set. In the second step, the q-quantile of this set is passed into a second set. The second set forms the set of ice-surface signal photons.

Mathematically, this reads as follows (summarized from [Herzfeld et al., 2017]):

Threshold-determination is carried out in along-track bins of size t_{bin}, with $t_{bin} = 5m$ for the melt-pond analysis in this paper. For each bin, indexed by s, the maximal value of density for all points in the noise slab $\mathcal{D}_{noise,s}$ for this bin is found according to

$$f_{max,noise,s} = max\{f_{d,a}(c) \mid c \in \mathcal{D}_{noise,s}\} \tag{5}$$

using eqn. 4 for the density value $f_{d,a}(c)$. Next a first threshold-value $t_{s,1}$ is calculated as

$$t_{s,1} = f_{max,noise,s} \; + \; t_{offset} \tag{6}$$

by adding a global threshold offset $t_{offset} \in \mathcal{R}$ to the maximal density value found in the noise slab.

We define the set $\mathcal{T}_s$ as the set of all photon returns (center points) c in the corresponding bin in the signal slab $\mathcal{D}_{signal,s}$ with density value larger than the first threshold $t_{s,1}$:

$$\mathcal{T}_s \;=\; \{f_{d,a}(c) \mid c \;\in \mathcal{D}_{signal,s} \wedge \; f_{d,a}(c) > t_{s,1}\} \tag{7}$$

A second threshold $t_{s,2}$ is defined as the q-quantile of the set $\mathcal{T}_s$, i.e. $t_{s,2} = v$ for the value v for which the density value satisfies

$$f_{d,a}(c) < v \tag{8}$$

for a fraction $0 \leq q \leq 1$ of the points c in the set $\mathcal{T}_s$.

Then a photon in bin s of the signal slab is identified as an ice-surface return if the density value of the photon is larger than the q-quantile of the set $\mathcal{T}_s$, i.e if

$$f_{d,a}(c) \;>\; t_{s,2} \tag{9}$$

defining the set of ice-surface returns in along-track bin s as

$$\mathcal{S}_s \;=\; \{c \mid c \in \mathcal{T}_s \;\wedge f_{d,a}(c) \;>\; t_{s,2}\} \tag{10}$$

The auto-adaptive thresholding process is illustrated in Fig. 2. The analysis uses $t_{offset} = 1$ and $q = 0.15$

The set of all ice-surface returns is the joint set of $\mathcal{S}_s$ for all along-track-bins

$$\mathcal{S} \;=\; \{c \mid c \in \mathcal{S}_s, s \in \mathcal{J}\} \tag{11}$$

for the index set $\mathcal{J}$ of all threshold-bin indices.

After application of the threshold function, surface height is given by the height values of individual photons that are classified as signal photons. The output of the threshold function has the same resolution as the original registered photons (without background photons), reported on ATL03, and therefore the spatial resolution of the output of the DDA-ice at this step is the same as the nominal 0.7, resolution of ATLAS. This is possible because the DDA-ice utilizes a data aggregation, not a data averaging operation.

Step 4. Roughness-controlled piece-wise linear ground follower. For users interested in surface height at a given location or users who prefer a continuous line of surface heights over heights at individual photon locations, a piecewise linear ground follower is applied. The terminology "roughness-controlled piece-wise linear ground follower" is a simplified description of a mathematical interpolator that builds on a segmentation of an interval into short sections where the surface is rough, and into larger sections where the surface is smooth. The height determination rules is summarized as follows: If standard deviation of the photons determined as signal photons (in step 3) in a given along-track segment of length R (here: $R = 10m$) exceeds a value S (the standard deviation for the ground follower), then the smaller stepsize, calculated as $\frac{R}{f}$ is used for the piecewise linear interpolator. The height determination employs a density-weighted interpolator (equation (30) in [Herzfeld et al., 2017]).

Determination of algorithm-specific parameters. Sensitivity studies. The values of the algorithm-specific parameters are determined in a sensitivity study. A sensitivity study is a step-wise optimization process, during which parameters are varied one at a time, holding the rest of the parameter set constant around a control parameter set (typically the last parameter set used in a successful data analysis). Once a new optimal solution is found, this is set as the control set, and a next iteration, varying each parameter, is carried out. Iterations are continued until a satisfactory parameter set has been determined, aided by experience in photon-counting lidar data analysis or validation data.

Data handling information. Version v18.0 of the DDA-ice-py3 allows processing of large files (entire ICESat-2 ATLAS granules). This is facilitated by so-called "chunking", an operation that loads segments of the data sets (here: 3000 m along-track). Chunking requires involved handling of data and intermediate algorithm results when passed to subroutines, to avoid effects at "chunk" boundaries. the mathematical details of the chunking algorithm developed specifically for the DDA-bif-seaice algorithm go beyond the objectives of this paper.

Photon data are read in as as:

$$(dt, lon, lat, elev)$$

Photon data are appended with distance along-track as:

$$(delta\_time, lon, lat, elev, distance)$$

F. Algorithm Steps of the DDA-bifurcate-seaice (DDA-bif-seaice)

The idea of a bifurcating algorithm is to identify locations where two geophysically valid surfaces exist, here, the top and bottom of a melt pond on sea ice. Two surfaces can clearly be identified in ICESat-2 data in some situations, but less clearly in others. Implementation of this simple concept as an automated algorithm has several complications, due to the complexity of (a) the melt ponding process and (b) the lidar observations (interactions of the lidar signal with complex cryospheric materials, including snow, ice, slush, water). As discussed in section (4.4), the cryospheric materials undergo a metamorphosis during the melt process, and the different material resulting from the stages of this metamorphosis result in different returns of the lidar signal, manifested in the spatial distribution of photons in the point cloud. The ATL03 data can show many stages of "ponds in the making". The question is then, at which stage should an algorithm identify two surfaces and call out a pond? Determination of the location of a bifurcation and rejoining point is a third problem.

Critical to these problems as part of an algorithm is the determination of spatial resolution. The current analysis uses a horizontal resolution of 25 m and a vertical bin size of 0.1 m in the bifurcation criterion, which strike a balance between the conflicting goals of finding enough signal photons to identify bifurcations, while avoiding false positives. Pond bottom depths (and ice-surface heights) are resolved at 5 m and 10 m along-track resolution for rough and smooth surfaces, respectively, with smallest detectable ponds of 15 m and 30 m widths. The values have been determined in sensitivity studies.

In the following section, we describe how the bifurcation algorithm for sea-ice data is interleaved into the DDA-ice-1. Algorithm steps already detailed for the DDA-ice-1 in section (4.5) are simply summarized. New algorithms steps specific to the DDA-bif-seaice are introduced here.

Algorithm steps of the DDA-bif-seaice are illustrated in Fig. 2. There, four examples are given to provide insights in the operation of the algorithm steps for different sea-ice environments, reflection situations, morphological complexities and for an outer beam (strong beam 3) compared to the near-nadir central beam (strong beam 2).

(Step 1) Large-scale separation of signal and noise slabs

The input to this step is the set of raw ICESat-2 ATLAS photons, also called the photon point cloud, seen in Fig. 2 (x-1, where x=a,b,c,d). The signal of the Earth surface, here the surface of sea ice, sea water or pond water, coincides with the height range of strongest reflectors. Separation of noise and signal slabs at large spatial scale is relatively robust and can be carried out using histograms. The result is shown in Fig. 2 (x-2).

(Step 2) Calculation of the density field using the radial basis function, *rbf*, for the signal slab and the noise slab (same as DDA-ice-1)

The density field is shown in Fig. 2 (x-3).

(Step 3) Operation of an auto-adaptive threshold function to separate noise and signal photons, using density as an additional dimension

At this point, the same threshold algorithm is run as in the DDA-ice-1, but with a lower quantile, currently $q = 0.15$ (see the Table of algorithm-specific parameters, Table 1), that passes more photons as candidates for examination in the following steps. Running the auto-adaptive threshold function creates a set of signal photons, denoted by $\mathcal{S}$ (eqn. 11). Note that $\mathcal{S}$ is a subset of the set of photons in the signal slab (for DDA-ice-1 and DDA-ice-bifurcate-seaice). With the lower quantile, the set $\mathcal{S}$ is not the set of ice-surface photons any more, but rather a set of photons which are candidates for melt-pond surface or bottom photons. Running the original threshold algorithm with a really low threshold serves to eliminate outlier photons. We call the resultant set the pre-signal set. The main thresholding will be applied at a later step in the melt-pond algorithm of the DDA-ice-bifurcate-seaice (see (Step 4)).

The operation of the auto-adaptive threshold function for the pre-signal set is illustrated in Fig. 2 (x-4), with the resultant pre-signal set shown in Fig. 2 (x-5).

(Step 4) Melt-pond detection: Bifurcation algorithm with additional auto-adaptive thresholding

The actual melt-pond detection comprises several steps. The result of these steps are shown in Fig. 2 (x-6). Building on the logic of the thresholding algorithm (Step 3), a new bifurcation algorithm with additional auto-adaptive thresholding is designed. The new algorithm for melt-pond detection is implemented in a function called *compute_threshold_melt_pond*, abbreviated as *ctmp*, applied to signal photons only, i.e. to photons in the set $\mathcal{S}$ that results from step 3. Note that *ctmp* is not applied to all photons in the signal slab, only to signal photons resultant from step 3. The function *ctmp* currently uses the same quantile, q, as the thresholding in step 3 (i.e. $q = 0.15$.)

The function returns the photon signal sets associated with the top surface and the bottom surface (if applicable); these are subsets of the pre-signal set from Step 3. In case only one surface is found, the result is identical to that of the DDA-ice-1 (with appropriate parameters).

(Step 4.1a) ctmp-1a: Calculate a vertical histogram of the signal photons

The bifurcation code begins by determining if two surfaces exist. A vertical histogram is calculated for the photons in the set $\mathcal{S}$ (at vertical resolution mp_bin_v), for every segment of a horizontal resolution mp_bin_h. Here, we use $mp\_bin_v = 0.1$ and $mp\_bin_h = 25$ (units in meters). All following steps are carried out for each horizontal step of resolution mp_bin_h.

(Step 4.1b) ctmp-1b: Apply a binomial filter to the histogram

Then the histogram, H, is filtered (or smoothed) using the Butterworth filter. In this simple form, it is a binomial filter. The new histogram counts H_{new} at vertical location x (or elevation), are given the value:

$$\begin{aligned} H_{new}(x) =& H(x-2)\cdot 0.0625 + H(x-1)\cdot 0.25 \\ &+ H(x)\cdot 0.375 + H(x+1)\cdot 0.25 \\ &+ H(x+2)\cdot 0.0625 \end{aligned} \tag{12}$$

For edge cases, one simply drops the term that are out of bounds. For example, for bin 0 we use:

$$H_{new}(0) = H(0)\cdot 0.375 + H(1)\cdot 0.25 + H(2)\cdot 0.0625 \tag{13}$$

(Step 4.2) ctmp-2: Find peaks in the filtered vertical histogram of signal photons

Peaks in the filtered vertical histogram will indicate reflectors, and if there is more than one reflector, a melt-pond may exist in the examined location. The determination of peak locations is currently implemented as a call to the *scipy* library function *find_peaks*, which is called with the maximum number of peaks set to 2. There are two cases possible: (1) If at least two peaks are found, then set $peak_1 = top$ and $peak_2 = bottom$ and apply the algorithm for the bifurcation case; and (2) If only one peak is found, then only one surface is identified. The scipy function also determines a saddle point (a minimum between the two peaks). The two cases of peak determination are illustrated in typical filtered histograms in Fig. 3; such histograms can be output by the DDA-bif-seaice as an option.

(1) If at least two peaks are found, then the algorithm finds the two largest peaks, where $pk1$ is the bin associated with the top surface and $pk2$ is the bin associated with the bottom surface. Next we find a specific histogram range, or a signal "slab", for each peak (or associated surface). We first find the minimum histogram bin between the two peaks pk_min, referred to as the saddle point. The number of the bins, or distance, between the saddle point and the peak for the top surface is called d. The slab associated with the higher surface

(top surface) is bounded below by saddle bin and above by $pk1 + d$. Thus the upper slab is centered at the peak $pk1$ with a size determined by the separation of the peak bin from the saddle-point bin between the two peaks. If the upper boundary is above the histogram limit, then the top of the slab boundary is set to the uppermost histogram bin. The second slab, associated with the lower surface, ranges from the saddle bin pk_min to the first bin below the second peak $pk2$ that drops to 0 signal photon counts. In this case of two identified surfaces (case 1), the function returns the two photon signal sets associated with the top and bottom surface, using $\mathcal{S}_{top}$ to denote the set of top (surface) photons and $\mathcal{S}_{bot}$ to denote the set of bottom photons.

The regular ground follower is then applied in a modified version to both signal sets $\mathcal{S}_{top}$ and $\mathcal{S}_{bot}$ to interpolate the two distinct surfaces (for each along-track bin). Note that in the code the ground follower is applied to the union of all the along track bins, i.e. the entire track, all at once. It uses the same quantile $dq = 0.75$ for both surfaces. The modified ground follower is described in (Step-5).

(2) There is also the case where only a single surface is identified (one peak returned from the *find_peaks* function with our parameterization). In this case, the threshold function acts as for DDA-ice-1 to return the thresholded photons to be interpolated by the ground follower. The code simply returns this same thresholded set of photons as the photon signal slab for both the top and bottom surfaces, which implies that the two surfaces would merge in the ground-follower (Step 5), formally, the same ground estimate is output for both surfaces for this particular horizontal or along-track bin. The ground follower is described in (Step 5) for this case as well.

(Step 4.3) ctmp-3: Create a set of bifurcation and rejoining points: A counter for discrete ponds

In this step, a set of bifurcation points and a set of rejoining points are created, which aid in keeping track of start and end locations of discrete ponds. This set is later examined in the melt-pond ground follower, which has the capability to function for pond regions and regions of a single surface. Numerically, the identification of bifurcation and rejoining points is carried out as part of (Step 4.2), changing the value of an indicator whenever a switch in the number of peaks occurs.

As a result of this step, we are able to carry out analyses of properties per pond, such as maximal and average pond depth and pond width.

(Step 5) Pond-specific surface follower

In step 5, a melt-pond specific surface follower is applied to both the top surface signal-photon set, $\mathcal{S}_{top}$, set and the bottom surface signal-photon set, $\mathcal{S}_{bot}$. The surface follower employs the same roughness-adaptive ground follower function, as described for the DDA-ice-1. Numerically, the ground-follower algorithm moves along-track, calculating surface heights for each segment for both surface sets. The melt-pond ground follower uses a melt-pond quantile, $dq = 0.75$. The role of the melt-pond quantile in the ground follower function is to "place" the reflector/ ground height at a certain percentile of the set of signal photons in the respective set (the set of surface signal photons or the set of bottom signal photons). In the current code version, the same melt-pond quantile $dq = 0.75$, is applied for both surfaces, but different quantiles could be used in a future version of the algorithm. There is also an option to place surface height at max density, which is not used in the current melt-pond analysis.

The same values of the ground-follower resolution, $R = 10[m]$, and the reduction factor for rough surfaces, $r = 2$, are employed for both surfaces, but one can be smooth (resulting in the 10m resolution) and the other one can be rough (resulting in the 5 m resolution). Typically, the pond bottom is rougher than the pond surface, but we do not force the pond surface to be flat at this point (because the top surface could also be a ridged surface between ponds).

The result of the surface follower is a set of piecewise linearly interpolated surface heights, $\mathcal{S}_{top-interp}$, and piecewise linearly interpolated bottom heights, $\mathcal{S}_{bot-interp}$.

Case 2. In case (2) [no pond], the algorithm works as follows: If no pond is detected (and between ponds, i.e. wherever only one surface exists), then the roughness-adaptive ground follower is applied, as described in Step-4 of the DDA-ice-1. This capacity creates a surface that follows ridges (rough sea-ice areas) with a smaller segmentation in the piece-wise ground follower, as well as smooth sea-ice, where a larger segmentation is used. (see, Table 1). The result of the surface follower is a set of piecewise linearly interpolated surface heights, $\mathcal{S}_{top-interp}$.

In case (1) [pond], an additional algorithm module for correction of melt-pond surface heights is applied (Step 6).

(Step 6) Correction of melt-pond surface heights and calculation of pond statistics

(Step 6.1) Correction of melt-pond surface heights

Case 1. In case (1) [pond], the surface follower

(a) makes the top surface flat and horizontal, and
(b) throws out false negatives.

For case (1), the following steps are carried out. This is implemented as running a "for" loop over the ponds, the following steps are carried out for each pond.

(Case 1.1). If the mean elevation of the surface is larger than the elevation of the pond edges plus a small value ϵ, then it is determined that de facto no pond exists: Calculate $m(s)$ as the mean of the surface height for the top of the pond, based on the heights of the photons in the top surface signal slab, and calculate the edge average as $a(e) = h((edge - left) + h(edge - right))/2$. Then apply the following criterion: If

$$m(s) > a(e) + \epsilon \tag{14}$$

then set top=bot.

This throws out false positives created by too small height differences.

Current value is $\epsilon = 0.2m$

(Case 1.2). If the two pond edges are very different in height, the set top=bot.

Current code uses:

$$|left\_edge - right\_edge| > 1 \tag{15}$$

This step throws out false positives created by ridge edges.

(Case 1.3). Min-width criterion: A minimum-width criterion is applied to map ponds. This requires that a least 3 depth

measurements are taken, i.e. the pond needs to have a minimal size of three segments of the ground follower.

Based on the ground follower resolution, the minimal pond size is 30 m for smooth surfaces, if length of piece-wise linear interpolator size is 10 m (see Table 1). Using $R = 2$ for the ratio of smooth to rough segment lengths in the ground follower, minimal pond size that is mapped is 15 m. That means, if the bottom is rough then we can find ponds of 15 m minimal size.

This can be interpreted as follows: If a pond formed on really rough ice and melting started and the sea-ice morphology was approximately preserved during subsiding, leading to rough pond bottoms, then we can identify 15 m wide ponds.

Notably, the along-track bin size of the ground follower can be smaller than the horizontal bin size of the bifurcation algorithm, because step 5 is applied to the signal photons in the bottom and top signal slabs.

(Step 6.2) Calculation of pond statistics

As the algorithm steps through the set of ponds, statistical values of interest to sea-ice scientists are calculated. These include:

1) pond width
2) maximal pond depth
3) average pond depth

Values of maximal and average pond depth are not corrected for the lower speed of light in water, compared to the speed of light in air. Atmospheric corrections on the ATL03 product account for the slightly lower speed of light in air, compared to he speed of light (in vacuum), see [Neumann et al., 2019].

(Step 6.3) Correction for speed of light in water

As an approximation, the range between the pond surface and the pond bottom can be multiplied by 1.3. (Water has a refractive index of 1.3, where the refractive index of vacuum is 1.0). This correction is currently applied outside of the DDA-bif-seaice in post-processing of pond depths.

Results of the pond statistics are utilized in the companion paper on evolution of melt ponding on Arctic seaice in the multi-year seaice region, including the Lincoln Sea (see, section 5); [Buckley et al., prep].

V. Application: Melt-Pond Detection in ICESat-2 ATLAS Data From the Multi-Year Arctic Sea-Ice Region

The DDA-bif-seaice was applied to ICESat-2 ATLAS data from the multi-year Arctic sea-ice region (MYASIR; Fig. 4) for the melting seasons (June - August) of 2019 and 2020. Results from 2019 are given in Fig. 1 and already discussed in section (3), focusing on illustration of pond detection capabilities (a) in different beams, (b) in different sea-ice environments, and (c) in various situations of background and signal strength. Now that the algorithm has been introduced, we take a closer look at examples that illuminate certain typical sea-ice morphological situations and problems of pond detection.

A. Ponds Among Ridges and in Complex Sea-Ice Topography

A frequently occurring morphological type of sea ice is that of faulted ice blocks. These form when compressive stress is applied to a sea-ice province, for example by wind, causing fracturing of the sea ice into blocks, which are then thrusted upward and can be partly pushed on top of each other. Melt ponds tend to form on the side of a faulted block. Detection of ponds aside fault blocks may provide useful information for modeling sea-ice physical processes at high resolution.

The example in Fig. 5a shows two ponds, which have surfaces at different heights and the two ponds are forming in two of the typical, but different, neighboring environments: Pond 1 (at 4400) is located among of sea-ice with a low topographic relief, that is relatively smooth to the left of pond 1 and somewhat ridged on the right of pond 1. A small fault block could be located immediately right of pond 1. Pond 2 (at 4600) is situated to the side of a fault block, where the fault block forms a ridge.

The surface follower is not optimized to follow the ridge topography in this code version (DDA-ice v18.0, Dec. 2021), resulting in unrealistically smoothed-out topography (Fig. 5a). Analysis of ridged and ponded areas with an older code version (DDA-ice v16.0, October 2021), which includes a different surface follower for single surfaces, renders ridge topography more realistically (Fig. 5b).

B. Results From Summer 2020 Data

For the 2019 data, analysis was carried out automatically detecting ponds which were already detected manually as well as with the UMD Melt-pond algorithm (thus ponds have pond identifiers), to provide a proof of concept. For the 2020 data, a large set of tracks (10% of all tracks collected) was processed for a large area of the Arctic. Results from 2020-July-13 data (Fig. 6) show ponds at different stages of formation and in different sea-ice environments, some of which are province types not previously illustrated in Fig. 1. Notably, total signal strength in examples Fig. 6a, b, c, d, e is significantly lower than in the 2019 examples presented, but higher for the examples in Fig. 7. The analysis for all 2019 and 2020 data was run using DDA-ice v18.0 with the same algorithm-specific parameter sets, given in Table 1, which further demonstrates the auto-adaptive capability of the algorithm. In Fig. 1h, a large pond neighbors small ponds that are correctly detected, as well as a region of dead-time effects that appropriately avoided.

Examples include the following: (a) A pond at an early stage of formation, located in smooth sea-ice area (Fig. 6a). Neighboring areas show penetration of ice with water, likely leading up to pond formation; (b) ponds among ridges at various formation stages (Fig. 6b); (c) a pond in a partly ridged, partly smooth area (Fig. 6c); (d) a pond in typical location near a ridge (Fig. 6d), as already described in section (5.1), (e) an unusually small pond at an early formation stage (Fig. 5e) and (f) a small pond that is detected. Notably, no false positives are detected in a high-density area between 665600 and 665800 (see, section 5.3); and (h) an unusually deep pond (approximately 4 m uncorrected depth, corresponding to 5.2 m corrected depth), that is situated between two small ponds (near 675600) and a region of high surface reflectance (density 350 or larger).

A physical interpretation of melt-pond evolution based on the results from analysis of large data sets over the MYASIR with the DDA-bif-seaice are reported in [Buckley et al., prep].

C. Avoidance of Saturated Signals

In situations of highly reflective sea-ice surfaces, the lidar signal received by the ATLAS sensor can become saturated. This means, that more photons are received than can be counted. As a result, a second range bin of photons will appear at a fixed range, or distance, determined by the detector dead-time. The first of these is 0.43 m below the saturated surface. For the central beam pair, whose beams are near-nadir pointing at the ice surface, saturation is relatively common over specular refrozen ponds or specular water surfaces of melt ponds. This effect creates a challenge in possible mis-classification of saturation effects as melt ponds, because the range of 0.43 m lies within the depth range of melt ponds. The dead-time effect leads to signals that are a fixed distance below the height of the primary surface and follow the shape of the primary surface. For pond surfaces, which are flat, the artifact surface is also flat (see, Fig. 7b). The dead-time effect can be persistent over long distances of the ICESat-2 ground tracks (see, Fig. 7a and 7b).

The DDA-ice-1 has the property to avoid secondary signals in most situations, simply because those are less dense than the primary surface. For the DDA-bif-seaice, the challenge is larger, because the goal is now to detect secondary surfaces that are weaker. In many cases, detection of false positives, misidentified as ponds, is avoided by the *cmtp* module of the algorithm, as illustrated in Fig. 6f (between 665600 and 665800), Fig. 6g (between 626600 and 626800). However, avoidance of misclassification of dead-time effect-generated secondary surfaces as false ponds is far from perfect, as seen in the example in Fig. 7a between 1.2064 and 1.2066, among otherwise correctly avoided secondary signals, while Fig. 7b gives and example of a strong saturation effect (density 400).

Data situations such as seen in Fig. 1d may benefit from a validation campaign (see, section 7), to distinguish between sections that may be dominated by saturation (dead-time effect), while the ponds in Fig. 1c and Fig. 1f have complex bottom topographies and thus are not saturation (dead-time) artifacts, despite the strong surface reflectance (density values of 200-250). Notably, the absolute density value is not a well-defined criterion for saturation, because the density value depends on the algorithm-specific parameters that control the kernel as well as on background intensity and because the threshold function is auto-adaptive.

An experimental algorithm to avoid saturation effects is in development, but not applied here. Because of the saturation problem, the analysis in [Buckley et al., prep] utilizes only results from the outer beams, pairs 1 and 3. Furthermore, the analysis in [Buckley et al., prep] was restricted to strong beams, because only a subset of all ICESat-2 tracks crossing the multiyear Arctic sea-ice region could be processed due to constraints of computer time on ADAPT and detection capability is better for strong beams than for weak beams in general.

The product ATL03 has flags for “saturated” and “near-saturated” signals, preliminary analysis indicates that these flags do not correlate well with saturation effects and do not provide a good solution for the saturation problem.

VI. Evaluation: Comparison to Results From ATL07 and From the UMD Melt-Pond Algorithm

A. Comparison to ICESat-2 ATLAS Sea-Ice Product ATL07

The ICESat-2 ATLAS sea-ice product ATL07 is not designed to detect two surfaces, hence melt ponds are not reported and in ponded regions the surface height on ATL07 may represent that of the surface or a value between the surface and the pond bottom [Farrell et al., 2020]. A few examples showing the information gain between ATL07 and results from the DDA-bif-seaice are given in Fig. 8. The results suggest inclusion of melt pond information on a future version of the ICESat-2 ATLAS products.

In regions without melt ponds, surface heights of ATL07 and from the DDA-bif-seaice are in good agreement, where surface topography is smooth or moderately rough, however in ridged areas the DDA ground follower needs to be revisited to better reflect high topographic relief (see, Fig. 5).

B. Comparison to Melt-Pond Depth Measurements Using the UMD Algorithm

In addition to visual interpretation of the photon cloud, results from several hundred manually identified ponds from the 2019 melt season were employed for evaluation of the DDA-bif-seaice results during early stages of algorithm development (Figure 8). The 2019 data analyses were re-run with the latest DDA algorithm version (v18.0) for inclusion in this paper. Ponds were visually identified in ICESat-2 ATLAS photon cloud data (ATL03 data) and computationally analyzed using the UMD Melt Pond Algorithm (MPA). To facilitate a study of evolution of melt ponds across the entire MYASIR, a representative subset (10%) of all ICESat-2 ATLAS data collected in this region in summer 2020 (June-August) was analyzed with the DDA-bif-seaice. The 2020 data analysis supports a statistical comparison of results from the two algorithms (Fig. 9).

1) Description of the University of Maryland Melt Pond Algorithm (MPA): The University of Maryland Melt Pond Algorithm (MPA) is a computational algorithm for detection of melt ponds in ICESat-2 ATLAS (ATL03) data that requires a-priori determination of the location where a pond exists, then centers the pond analysis on the middle of the pond and computes the depth of the pond in increments. Control points at the pond bottom can be added. The MPA is described in detail in [Buckley et al., prep] and a brief description is included here. The MPA was developed to track the melt pond surface and bathymetry in the ATL03 photon cloud. We examined cloud free areas and manually identified melt ponds in the photon cloud. In the ATL03 photon cloud, melt ponds present as a level surface, and a bowl-shaped bathymetry with minimal photons return between these two surfaces. We note the start and end of a pond as the point at which the two surfaces become distinguishable. Across the pond, we bin photons into 0.1 m vertical bins and find the surface as the mode of the binned distribution. Next, the photons are binned into 10 m along-track bins, and 0.1 m vertical bins. For each 10 m along-track segment we locate modes below the surface that have at least 5% of the surface photons. The subsurface mode closest to the surface is associated with the reflections from the bottom of the pond and the bathymetry is defined as the vertical bin elevation of this mode. Bathymetry is determined in this way for each of the 10 m along-track segments. To determine melt pond depth, we subtract the secondary surface that tracks the melt pond bathymetry from the primary surface that tracks the melt pond surface. However, the ATL03 algorithm does not account for the change of the speed of light in water when determining the geolocation of the photons. To determine the correct melt pond depth, we multiply the uncorrected depth by the ratio of the speed of light in water to the speed of light in air (0.749). To increase the along-track resolution, we interpolate the pond depths at 5 m increments.

2) Comparison of Retrieval Results From the MPA and the DDA-bif-seaice: To compare results from the two algorithms, the UMD MPA and the DDA-bif-seaice, statistically, we examine retrieved average surface heights and surface widths for the 113 ponds that both algorithms tracked. The statistical analysis utilizes DDA-derived heights resampled at 5 m increments for consistency with MPA-derived heights (rather than average height and width values output by the DDA directly). For each pond, we determine the mean pond depth and plot MPA and DDA mean pond depth (as seen in Fig. 8e, f). We find the algorithms in good agreement, with a correlation value of 0.77, a mean difference of -0.04 m (DDA-MPA; i.e. the bottom height is generally lower in the DDA-bif-seaice results) (Fig. 9). The standard deviation of the residuals is 0.22 m. The difference in depth retrievals between the two algorithms is attributed to the different physical-mathematical philosophies regarding the interaction of light with the cryospheric materials at the bottom of a pond (see, Fig. 8e,f); further work on this requires field validation (see section 7).

The DDA-bif-seaice can detect ponds of a minimal size of a nominal size of 15 m (for rough areas or pond bottoms) and of 30 m (for smooth areas or pond bottoms). While these values are algorithm constraints, the detailed analysis of melt-pond evolution in [Buckley et al., prep] demonstrates that the DDA-bif-seaice facilitates detection of a multiple of the number of ponds compared to the UMD MPA. As seen in Fig. 4, the DDA-bif-seaice detected approximately 10200 ponds. The statistics of the pond sizes in the referenced study shows that the size range of ponds detected with the DDA-bif-seaice is much larger including large ponds of several hundred meters width as well as ponds of tens of meters width, whereas the MPA finds only large ponds (as may be expected from a manually forced detection). For both algorithms, melt-pond size is found to increase as melting progresses early in the season. This again is likely explained by the ability of the DDA-bif-seaice to detect narrow, shallow ponds. The agreement in trends is sufficient to support physical interpretation of melt-pond processes in the Arctic [Buckley et al., prep]. Because of the general agreement of pond location and depth trend for the ponds detected in both algorithms, the DDA-bif-seaice has the capabilities expected from a fully automated algorithm for melt-pond detection in ICESat-2 ATLAS data.

VII. Discussion and Outlook

The DDA-bifurcate-seaice has been successfully applied to automated detection of ponds and measurement of their depth and extension, as demonstrated in this paper and in the applied companion paper [Buckley et al., prep].

The evaluation of the DDA-bif-seaice in this paper has been carried out by application of satellite data analysis and comparison to results from another, also unvalidated, algorithm. Depth determination builds on experience gained in analysis of water in crevasses, observed during an ICESat-2 airborne validation campaign over the Negribreen Glacier System, and on heuristics and sensitivity studies [Herzfeld et al., 2022]. Systematic differences in pond depth between results from the UMD MPA and the DDA-bif-seaice are attributable to different philosophies applied in the rules for "placing" the surface and pond bottom heights within the photon cloud [Buckley et al., prep].

Close scrutiny of the four examples of "megaplots" (Fig. 2, threshold function panels (x-4)) shows that large numbers of photons pass in regions of ponds that are characterized by weakly reflecting pond surfaces with clear pond interiors, indicating melt/slush at and below the bottom of the ponds (Figure 2 a,b). In contrast, ponds with strongly reflecting surfaces (perhaps refrozen water) have vertically narrower sets of signals at or near the pond bottom, which might indicate a colder, less slushy environment (Fig. 2c, d). The DDA-bif-seaice is controlled by an algorithm-specific set of parameters. The exact optimization of these parameters to identify pond bottom heights within the lower set of signal photons requires validation data from a field campaign. On the other hand, the thought experiments that can be carried out with the mere photon data alone already suggest a wealth of information on the cryo-materials (firn/slush/ice/water) is captured in the ICESat-2 photon data and their density field.

For this paper, the algorithm-specific parameter set for the DDA-bif-seaice has been determined by preliminary sensitivity studies, which are a a form of mathematical optimization that utilizes iterative steps. Effects of parameter changes on detection and measurement results are analyzed, using variation of parameters around evolving control parameter sets [Herzfeld et al., 2017]. This process leaves uncertainties in depth and width determination of ponds. Actual uncertainties determined in sensitivity studies are on the order of $\pm 0.2m$, which when integrated over a large part of the Arctic oceans are significant enough to warrant further study. For comparison, an average systematic difference in 0.44 m with a standard deviation of 0.22 m was found between results from DDA-bif-seaice and UMD MPA ponds for 113 larger ponds identified by both algorithms in this study. Critical is the penetration of the lidar signal into complex marine cryospheric media, which include, in addition to ice and water, snow on top of the sea ice, snow during metarmorphosis, firn, slush, sea water, and brine. As is well-known [Smith et al., 2018], the penetration depends on frequency. The average ice-surface height difference from red and green lidar data is on the order of 0.15 m (with heights from green laser data generally lower) and standard deviation 0.23 m [Herzfeld et al., 2017], but specifics depend on the cryomaterials and there are many unknowns. Airborne field data, including red and green lidar data and high-resolution image data, were collected during the ICESat-2 Arctic summer sea-ice campaign in July 2022. These data, once processed and analyzed, may provide constraints for optimization of the algorithm-specific parameter set of the DDA-bif-seaice and thus may allow a reduction of uncertainty in depth estimation.

VIII. Summary and Conclusions

The importance of understanding melt processes in the Arctic sea ice in the current realm of climatic warming motivates development of an advanced mathematical algorithm for detection of ponds in ICESat-2 Advanced Topographic Laser Altimeter System (ATLAS) data. In this paper, we introduce the Density-Dimension Algorithm for bifurcating sea-ice reflectors (DDA-bifurcate-seaice or DDA-bif-seaice for short), an algorithm that facilitates automated detection of melt ponds in ICESat-2 ATLAS data, retrieval of two surface heights, pond surface and bottom, and measurements of depth and width of melt ponds.

The ATLAS instrument is the first space-borne multi-beam micro-pulse photon-counting laser altimeter system, it operates at 532 nm (green light) frequency and registers returns from every single photon in the green-light domain of the sensor. Data are reported in the ICESat-2 ATLAS geolocated photon point cloud product, ATL03. ICESat-2 ATLAS data resolve returns from top and bottoms of melt ponds in the photon point cloud, but because of the high background especially during daylight conditions, separation of noise and signal and especially detection of two surfaces of typically different intensities are mathematically ill-posed problems.

The DDA-bifurcate-seaice is an auto-adaptive algorithm that solves the problem of pond detection at the 0.7m nominal resolution of ATLAS data. The DDA-bif-seaice builds on the Density-Dimension Algorithm for ice surfaces (DDA-ice), utilizing the radial basis function for calculation of a density field and a threshold function that automatically adapts to changes in background, apparent surface reflectance (ASR) and some instrument effects. The centerpiece of the DDA-bif-seaice is a bifurcation module, designed to satisfy the following criteria for a melt-pond algorithm for analysis of point cloud data of lidar data: (1) The algorithm needs to be fully automated (i.e. it should not require a-priori information on the existence or location of a pond), (2) detect ponds wherever they exist and (3) avoid false positives, (4) automatically adapt to different background characteristics of daytime and nighttime data and to changes in ASR, (5) find ponds among sea-ice of different roughness types (smooth, ridged, and complex), (6) correctly determine the start and end points of a pond along the ICESat-2 ground track, (7) measure the pond depth, and (8) represent the complexity of the sea-ice at high resolution. The DDA-bif-seaice includes a ground follower that automatically adapts to roughness of pond surface and pond bottom (or of a single surface where no ponds exist). Smallest width of detectable ponds is 15 m for rough surfaces and 30 m for smooth surfaces, currently used height resolution is 0.1 m. Ponds can be identified in typical locations aside ridges formed by fault blocks and in other complex environments. Its computational efficiency suggests that a future version of the DDA-bif-seaice may be applied as an operational algorithm for analysis of ICESat-2 ATLAS data across large regions, including the entire Arctic and Antarctic sea-ice regions. The problem of signal saturation is explained and needs to be addressed in future algorithm development, as currently saturation effects are partly avoided, but can also lead to false positives especially in near-nadir central beams.

Melt ponds are not reported on the standard ICESat-2 ATLAS sea-ice products ATL07 (sea-ice surface heights) and ATL10 (sea-ice freeboard), because of the low, 25 km along-track resolution of the products and because the ATL07 algorithm is designed to determine a single surface height. To illustrate the increase in information, results from the DDA-bif-seaice are compared to results from the ATL07 algorithm. Because ATL10 results are derived from ATL07, ponded areas can be mistaken for open water and thus freeboard miscalculated. Results from an advanced version of the DDA-bif-seaice analysis may be included in a future version of the standard ICESat-2 ATLAS data products.

To demonstrate the capabilities of the DDA-bif-seaice as a fully automated algorithm for melt-pond detection that automatically adapts to changing background conditions, especially to the more challenging conditions of daylight, the DDA-bifurcate-seaice is applied to large ICESat-2 data sets from the 2019 and 2020 melt seasons in the multi-year Arctic sea-ice region (MYASIR). The analysis is carried out for about 10% of all ICESat-2 data collected in summer 2020 (outer strong beam data), which is considered representative of the entire ICESat-2 ATLAS data set for this time frame and area. The results from the 2020 analysis yield approximately 10200 ponds and are utilized in a large-scale study on the evolution of melt ponding [Buckley et al., prep].

As a means of evaluation, results from the DDA-bif-seaice are compared to and integrated with results from the University of Maryland (UMD) Melt-Pond Algorithm (MPA), which is a computational algorithm for pond determination and depth measurement that requires a-priori, manually determined information on locations where melt ponds exist. Agreement in pond location between the two algorithms is generally good. The DDA-bif-seaice finds a large multitude of the number ponds compared to the UMD MPA with sizes across all size ranges, while the MPA aids in finding larger, deeper ponds. A systematic difference of about 0.44 m in pond depths, with DDA depths generally larger, attributed to different physical-mathematical principles in lidar data analysis in the two algorithms, indicates that a field validation campaign is needed to resolve such depth uncertainties. Agreement is sufficient for geophysical interpretation of trends in the pond evolution. The comparison further documents that the DDA-bif-seaice meets the criteria expected from a fully automated algorithm.

REFERENCES

[Buckley, 2022] Buckley, E. (2022). *High resolution remote sensing observations of summer sea ice*. PhD thesis, University of Maryland.

[Buckley et al., 2020a] Buckley, E., Farrell, S., Duncan, K., and Herzfeld, U. (2020a). ICESat-2 observations of melt ponds on Arctic sea ice. *American Geophysical Union Fall Meeting, 7-11 December 2020*.

[Buckley et al., 2019] Buckley, E., Farrell, S., Duncan, K., Herzfeld, U., and Webster, M. (2019). Sea ice melt pond properties as observed by ICESat-2. *American Geophysical Union Fall Meeting, San Francisco, CA, 9-13 December 2019*.

[Buckley et al., 2020b] Buckley, E. M., Farrell, S. L., Duncan, K., Connor, L. N., Kuhn, J. M., and Dominguez, R. T. (2020b). Classification of sea ice summer melt features in high-resolution icebridge imagery. *Journal of Geophysical Research: Oceans*, 125(5):e2019JC015738.

[Buckley et al., prep] Buckley, E. M., Farrell, S. L., Herzfeld, U. C., Trantow, T. M., Baney, O. N., Duncan, K., and Lawson, M. (prep). Observing the evolution of summer melt on multiyear sea ice with ICESat-2 and Sentinel-2.

[Farrell et al., 2020] Farrell, S., Duncan, K., Buckley, E., Richter-Menge, J., and Li, R. (2020). Mapping sea ice surface topography in high fidelity with ICESat-2. *Geophysical Research Letters*, 47(21):e2020GL090708, DOI: 10.1029/2020GL090708.

[Fricker et al., 2020] Fricker, H. A., Arndt, P., Brunt, K., Tri Datta, R., Fair, Z., Jasinski, M., Kingslake, J., Magruder, L., Moussavi, M., Pope, A., Spergel, J., Stoll, J., and Wouters, B. (2020). Icesat-2 meltwater depth estimates: Application to surface melt on amery ice shelf, east antarctica. *Geophysical Research Letters*, 48, DOI: 10.1029/2020GL090550.

[Herzfeld et al., 2021a] Herzfeld, U., Hayes, A., Palm, S., Hancock, D., Vaughan, M., and Barbieri, K. (2021a). Detection and Height Measurement of Tenuous Clouds and Blowing Snow in ICESat-2 ATLAS Data. *Geophysical Research Letters*, 48, DOI: 10.1029/2021GL093473.

[Herzfeld et al., 2014] Herzfeld, U., McDonald, B., Wallin, B., Markus, T., Neumann, T., and Brenner, A. (2014). An algorithm for detection of ground and canopy cover in micropulse photon-counting lidar altimeter data in preparation of the ICESat-2 mission. *IEEE Transactions Geoscience and Remote Sensing*, 54(4):2109–2125, DOI: 10.1109/TGRS.2013.2258350.

[Herzfeld et al., 2021b] Herzfeld, U., Palm, S., Hancock, D., Hayes, A., and Barbieri, K. (2021b). *ICESat-2 Algorithm Theoretical Basis Document for the Atmosphere, Part II: Detection of Atmospheric Layers and Surface Using a Density Dimension Algorithm, v13.0, November 15, 2021, Geomath Code Version v118.0, ASAS Code Release v5.5, ATLAS Data Product ATL09*. NASA ICESat-2 Project, DOI: 10.5067/48PJ5OUJOP4C. 439p.

[Herzfeld and Trantow, prep] Herzfeld, U. and Trantow, T. (prep). NASA's ICESat-2 Measures Summer's Crevasses on an Arctic Surge Glacier Through Winter's Snow Cover. *IEEE Transactions on Geosciences and Remote Sensing*.

[Herzfeld et al., 2017] Herzfeld, U., Trantow, T., Harding, D., and Dabney, P. (2017). Surface-height determination of crevassed glaciers — Mathematical principles of an Auto-Adaptive Density-Dimension Algorithm and validation using ICESat-2 Simulator (SIMPL) data. *IEEE Transactions in Geoscience and Remote Sensing*, 55(4):1874–1896, DOI: 10.1109/TGRS.2016.2617323.

[Herzfeld et al., prep] Herzfeld, U., Trantow, T., and Hayes, A. (prep). Water on ice — its detection, measurement and role in understanding cryospheric change processes – the view of icesat-2. *Geophysical Research Letters*.

[Herzfeld et al., 2021c] Herzfeld, U., Trantow, T., Lawson, M., Hans, J., and Medley, G. (2021c). Surface heights and crevasse types of surging and fast-moving glaciers from ICESat-2 laser altimeter data — Application of the density-dimension algorithm (DDA-ice) and validation using airborne altimeter and Planet SkySat data. *Science of Remote Sensing*, 3:1–20, DOI: 10.1016/j.srs.2020.100013.

[Herzfeld et al., 2022] Herzfeld, U. C., Lawson, M., Trantow, T., and Nylen, T. (2022). Airborne Validation of ICESat-2 ATLAS Data Over Crevassed Surfaces and Other Complex Glacial Environments: Results From Experiments of Laser Altimeter and Kinematic GPS Data Collection From a Helicopter Over a Surging Arctic Glacier (Negribreen, Svalbard). *Remote Sensing*, 14:1185–1224, DOI: 10.3390/rs14051185.

[Herzfeld et al., 2006] Herzfeld, U. C., Maslanik, J. A., and Sturm, M. (2006). Geostatistical characterization of snow-depth structures on sea ice near point Barrow, Alaska- A contribution to the AMSR-Ice03 field validation campaign. *IEEE Transactions on Geoscience and Remote Sensing*, 44(11):3038–3056, DOI: 10.1109/TGRS.2006.883349.

[Hunke et al., 2013] Hunke, E. C., Lipscomb, W. H., Turner, A. K., Jeffery, N., and Elliott, S. (2013). Cice: the los alamos sea ice model, documentation and software, version 5.0. *Los Alamos National Laboratory Technical Report*, (LA-CC-06-012), http://oceans11.lanl.gov/trac/CICE/attachment/wiki/WikiStart/cicedoc.pdf?format=raw.

[Jahn et al., 2011] Jahn, A., Sterling, K., Holland, M., Kay, J., Maslanik, J., Bitz, C., Bailey, D., Stroeve, J., Hunke, E., Lipscomb, W., and Pollak, D. (2011). Late 20th century simulation of Arctic sea ice and ocean properties in the CCSM4. *J. Climate*.

[Kay et al., 2011] Kay, J. E., Holland, M. M., and Jahn, A. (2011). Inter-annual to multi-decadal arctic sea ice extent trends in a warming world. *Geophysical Research Letters*, 38(15).

[Kwok, 2018] Kwok, R. (2018). Arctic sea ice thickness, volume, and multiyear ice coverage: losses and coupled variability (1958–2018). *Environmental Research Letters*, 13(10):105005.

[Kwok et al., 2019a] Kwok, R., Kacimi, S., Markus, T., Kurtz, N., Studinger, M., Sonntag, J., Manizade, S., Boisvert, L., and Harbeck, J. (2019a). ICESat-2 Surface Height and Sea Ice Freeboard Assessed With ATM Lidar Acquisitions From Operation IceBridge. *Geophysical Research Letters*, 46(20):11228–11236.

[Kwok et al., 2019b] Kwok, R., Markus, T., Kurtz, N., Petty, A., Neumann, T., Farrell, S., Cunningham, G., Hancock, D., Ivanoff, A., and Wimert, J. (2019b). Surface height and sea ice freeboard of the Arctic Ocean from ICESat-2: Characteristics and early results. *Journal of Geophysical Research: Oceans*.

[Kwok et al., 2019c] Kwok, R., Markus, T., Kurtz, N., Petty, A., Neumann, T., Farrell, S., Cunningham, G., Hancock, D., Ivanoff, A., and Wimert, J. (2019c). Surface height and sea ice freeboard of the Arctic Ocean from ICESat-2: Characteristics and early results. *Journal of Geophysical Research: Oceans*, 124(10):6942–6959.

[Kwok et al., 2021a] Kwok, R., Petty, A., Bagnardi, M., Wimert, J., Cunningham, G., Hancock, D., Ivanoff, A., and Kurtz, N. (2021a). *ICESat-2 Algorithm Theoretical Basis Document for Sea Ice Products, November 30, 2021*. NASA ICESat-2 Project, DOI: 10.5067/189WL8W8WRH8. 129p.

[Kwok et al., 2021b] Kwok, R., Petty, A., Cunningham, G., Markus, T., Hancock, D., Ivanoff, A., Wimert, J., Bagnardi, M., and Kurtz, N. (2021b). ATLAS/ICESat-2 L3A Sea Ice Freeboard, Version 5. DOI: 10.5067/ATLAS/ATL10.005. Boulder, Colorado USA.

[Kwok et al., 2021c] Kwok, R., Petty, A., Cunningham, G., Markus, T., Hancock, D., Ivanoff, A., Wimert, J., Bagnardi, M., and Kurtz, N. (2021c). ATLAS/ICESat-2 L3A Sea Ice Height, Version 5. DOI: 10.5067/ATLAS/ATL07.005. Boulder, Colorado, USA.

[Magruder et al., 2021] Magruder, L., Neumann, T., and Kurtz, N. (2021). ICESat-2 early mission synopsis and observatory performance. *Earth and Space Science*, 8, DOI: 10.1029/2020EA001555.

[Markus et al., 2017] Markus, T., Neumann, T., Martino, A., Abdalati, W., Brunt, K., Csatho, B., Farrell, S., Fricker, H., Gardner, A., Harding, D., et al. (2017). The Ice, Cloud, and land Elevation Satellite-2 (ICESat-2): Science requirements, concept, and implementation. *Remote Sensing of Environment*, 190:260–273, DOI: 10.1016/j.rse.2016.12.029.

[Maslanik et al., 2006] Maslanik, J., Sturm, M., Belmonte, M., Cavalieri, D., Gasiewski, A., Heinrichs, J., Herzfeld, U., Holmgren, J., Klein, M., Markus, T., Perovich, D., Sonntag, J., Stroeve, J., and K.Tape (2006). Spatial variability of Barrow-area shore-fast sea ice and its relationships to passive microwave emissivity. *Geoscience and Remote Sensing, IEEE Transactions on*, 44(11):3021–3031, DOI: 10.1109/TGRS.2006.879557.

[Neumann et al., 2021a] Neumann, T., Brenner, A., Hancock, D., Robbins, J., Saba, J., Gibbons, A., Lee, J., Luthcke, S., and Rebold, T. (2021a). ATLAS/ICESat-2 L2A Global Geolocated Photon Data, Version 5. DOI: 10.5067/ATLAS/ATL03.005. Boulder, Colorado USA.

[Neumann et al., 2021b] Neumann, T., Brenner, A., Hancock, D., Robbins, J., Saba, J., Harbeck, K., Gibbons, A., Lee, J., Luthcke, S., and Rebold, T. (2021b). *ICESat-2 Algorithm Theoretical Basis Document for Global Geolocated Photons ATL03, release 005, 2021*. NASA ICESat-2 Project, DOI: 10.5067/D0VQW9KX3GTU. 208p.

[Neumann et al., 2019] Neumann, T. A., Martino, A. J., Markus, T., Bae, S., Bock, M. R., Brenner, A. C., Brunt, K. M., Cavanaugh, J., Fernandes, S. T., Hancock, D. W., et al. (2019). The Ice, Cloud, and Land Elevation Satellite–2 mission: A global geolocated photon product derived from the Advanced Topographic Laser Altimeter System. *Remote Sensing of Environment*, 233:111325, DOI: 10.1016/j.rse.2019.111325.

[Notz and Community, 2020] Notz, D. and Community, S. (2020). Arctic sea ice in CMIP6. *Geophysical Research Letters*, 47(10):e2019GL086749.

[Palm et al., 2021] Palm, S., Yang, Y., Herzfeld, U., Hancock, D., Hayes, A., Selmer, P., Hart, W., and Hlavka, D. (2021). ICESat-2 atmospheric channel description, data processing and first results. *Earth and Space Sciences*, DOI: 10.1029/2020EA001470.

[Perovich et al., 2003] Perovich, D., Greenfell, T., Richter-Menge, J., Light, B., Tucker, W. B. I., and Eicken, H. (2003). Thin and thinner: Sea ice mass balance measurements during SHEBA. *Journal of Geophysical Research*, 108(C3):SHE–26, DOI: 10.1029/2001JC001079.

[Petty et al., 2018] Petty, A. A., Stroeve, J. C., Holland, P. R., Boisvert, L. N., Bliss, A. C., Kimura, N., and Meier, W. N. (2018). The Arctic sea ice cover of 2016: a year of record-low highs and higher-than-expected lows. *The Cryosphere*, 12(2):433–452.

[Scott and Feltham, 2010] Scott, F. and Feltham, D. L. (2010). A model of the three-dimensional evolution of Arctic melt ponds on first-year and multiyear sea ice. *Journal of Geophysical Research*, 115(C12064):37, DOI: 10.1029/2010JC006156.

[Serreze et al., 2007] Serreze, M., Holland, M., and Stroeve, J. (2007). Perspectives on the Arctic's shrinking sea-ice cover. *science*, 315(5818):1533.

[Serreze et al., 2008] Serreze, M., Meier, W., Stroeve, J., Scambos, T., and Renfrow, S. (2008). Arctic Sea ice in 2008: Standing on the threshold. In *AGU Fall Meeting Abstracts*, volume 1, page 01.

[Smith et al., 2018] Smith, B. E., Gardner, A., Schneider, A., and Flanner, M. (2018). Modeling biases in laser-altimetry measurements caused by scattering of green light in snow. *Remote Sensing of Environment*, 215:398–410.

[Stroeve et al., 2007] Stroeve, J., Holland, M., Meier, W., Scambos, T., and Serreze, M. (2007). Arctic sea ice decline: Faster than forecast. *Geophysical Research Letters*, 34(9):9501, DOI: 10.1029/2007GL029703.

[Stroeve and Notz, 2018] Stroeve, J. and Notz, D. (2018). Changing state of arctic sea ice across all seasons. *Environmental Research Letters*, 13(10):103001.

[Stroeve et al., 2012] Stroeve, J. C., Serreze, M. C., Holland, M. M., Kay, J. E., Maslanik, J., and Barrett, A. P. (2012). The Arctic's rapidly shrinking sea ice cover: a research synthesis. *Clim. Change*, 110:1005–1027.

[Sturm et al., 2006] Sturm, M., Maslanik, J. A., Perovich, D. K., Stroeve, J. C., Richter-Menge, J., Markus, T., Holmgren, J., Heinrichs, J. F., and Tape, K. (2006). Snow depth and ice thickness measurements from the Beaufort and Chukchi Seas collected during the AMSR-Ice03 campaign. *Geoscience and Remote Sensing, IEEE Transactions on*, 44(11):3009–3020.

[Tilling et al., 2020] Tilling, R., Kurtz, N., Bagnardi, M., Petty, A., and Kwok, R. (2020). Detection of Melt Ponds on Arctic Summer Sea Ice From ICESat-2. *Geophysical Research Letters*, 47(23):e2020GL090644.

IX. FIGURES

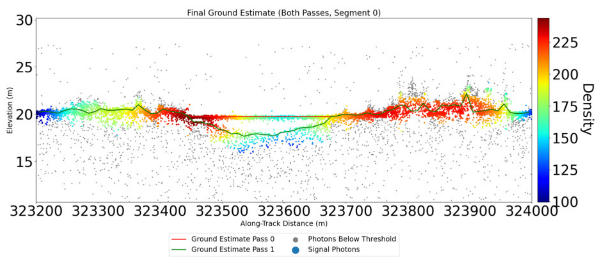

(a) 1237_gt3l_82.818.png [mega 3]

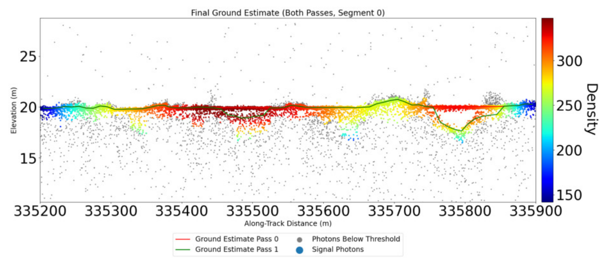

(b) 1237_gt1l_82.906.png

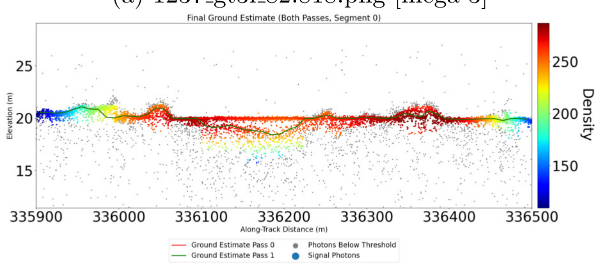

(c) 1237_gt1l_82.906_2.png

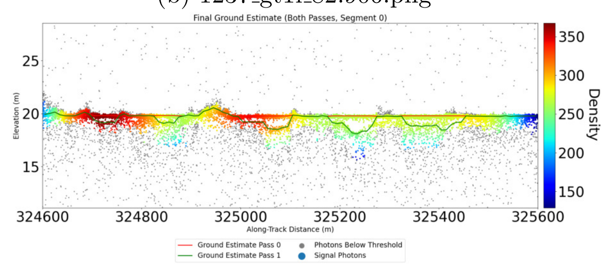

(d) 1237_gt3l_82.831.png [mega 4]

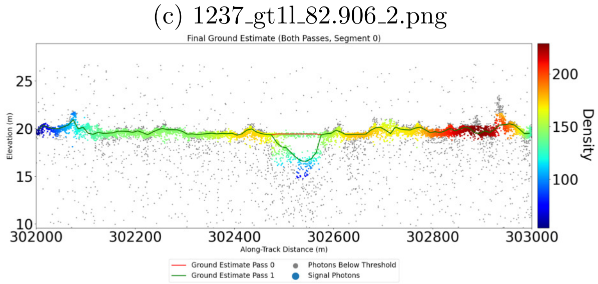

(e) 1298_gt3l_82.637.png [mega 1]

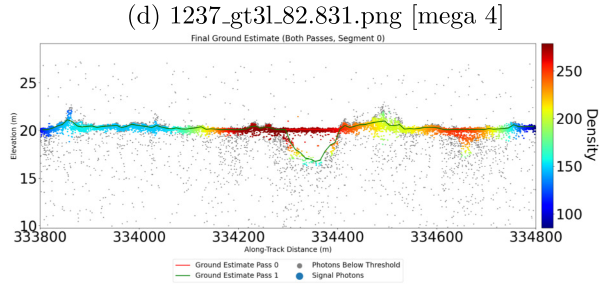

(f) 1298_gt3l_82.911.png [mega 2]

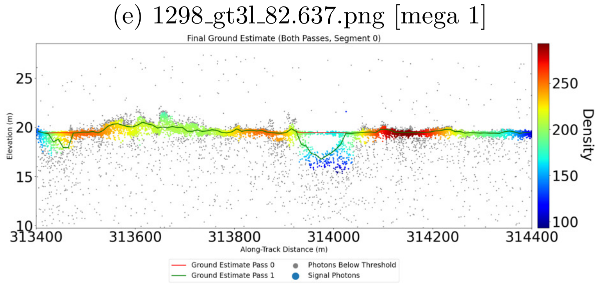

(g) 1298_gt2l_82.727.png

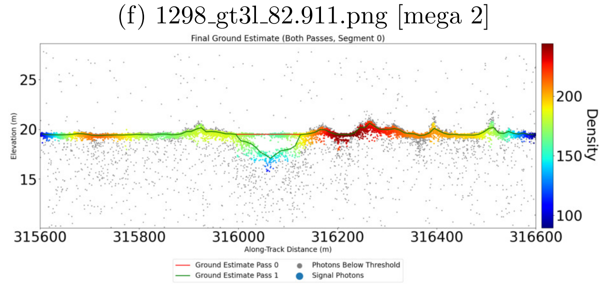

(h) 1298_gt2l_82.745.png

Fig. 1. Examples of ponds detected with the DDA-bif-seaice in summer 2019 ICESat-2 ATLAS data, Multi-year Arctic sea-ice region. Lincoln Sea. All ponds from strong beam data. (a) Pond among ridges with variable density at top. Surface follower (top) not optimized for ridges. (b) Several ponds detected - shows bifurcation and rejoining points. (c) Not a false positive - bottom of pond has variable topography. (d) complex regions with several ponds. Note rightmost pond is barely a pond in the making. (e) perfect pond. (f) perfect pond below strongly reflecting surface (density 250). (g) pond among complex sea-ice topography. Center beam (gt2l). (h) pond among complex sea-ice topography. Center beam (gt2l). Examples in 1a, b, c, d, e are from ICESat-2 ATLAS granule ATL03_20190618062235_12370304_005_01.h5, reference ground track (RGT) 1237, collected 2019-June-18, ICESat-2 ASAS version 5 data set. Examples in 1f, g ,h are from ICESat-2 ATLAS granule ATL03_20190622061415_12980304_005_01.h5, RGT 1298, collected 2019-June-22, ICESat-2 ASAS version 5 data set.

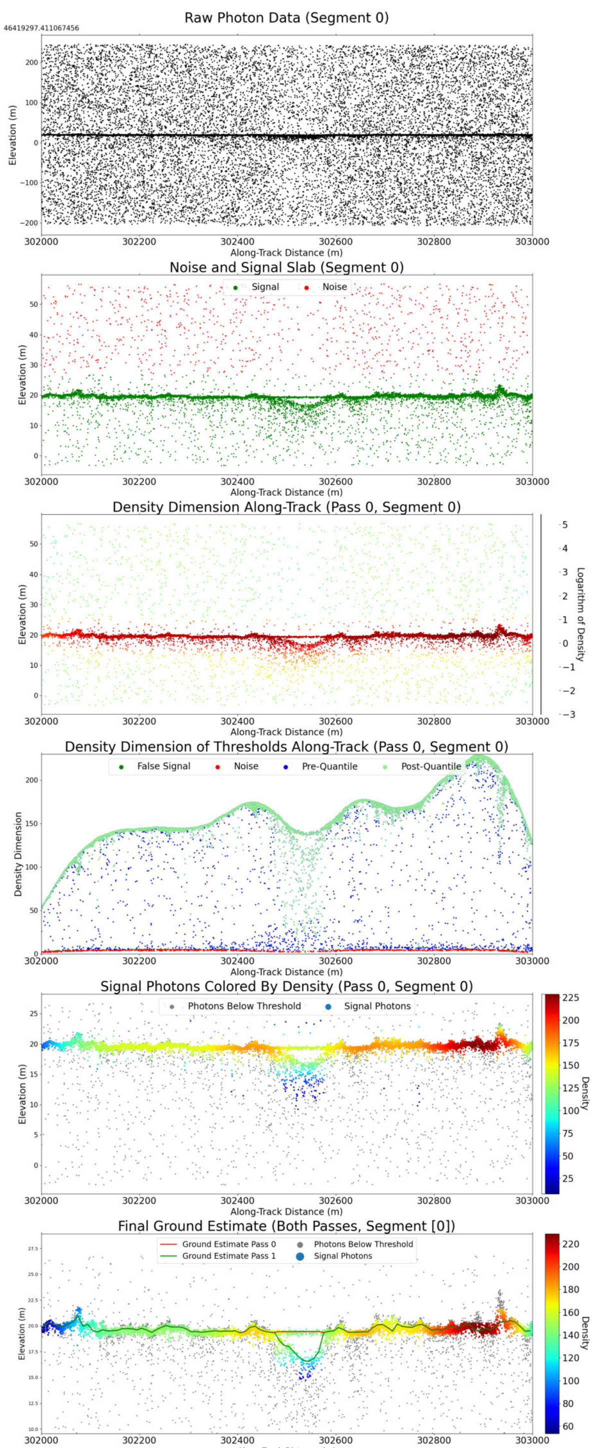

(a) 1298_gt3l_82.637.png [mega 1]

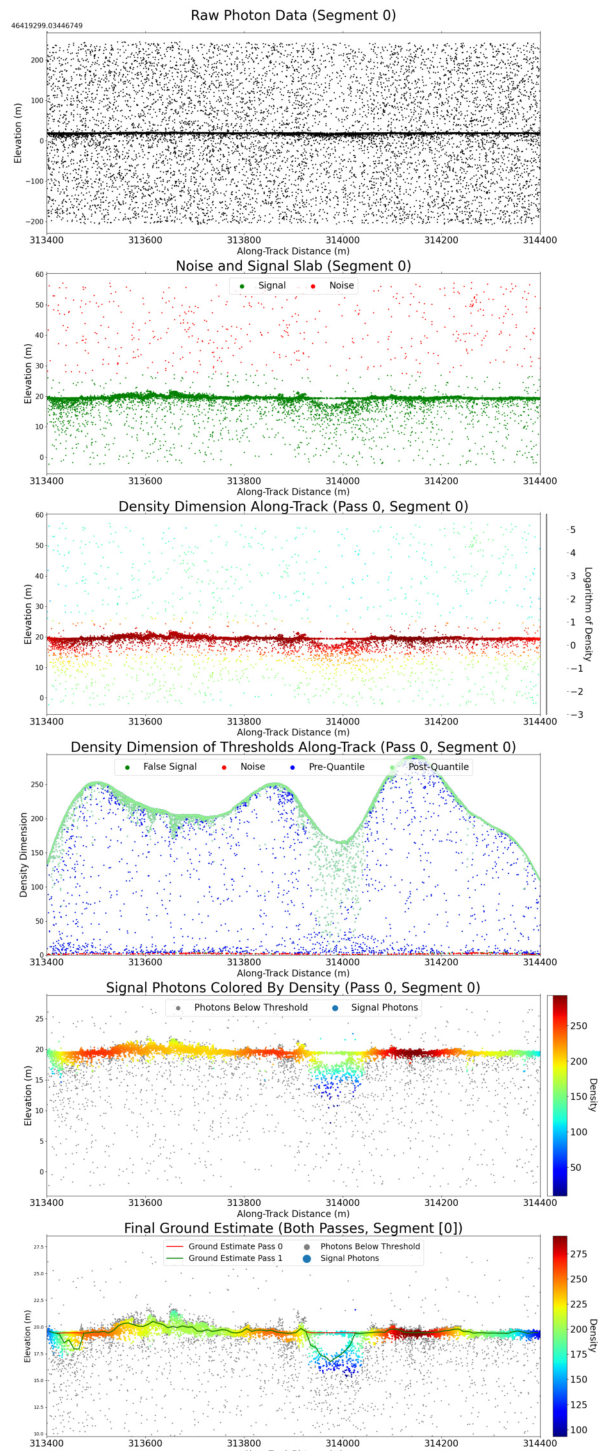

(b) 1298_gt2l_82.727.png [mega 2]

Figure 2. Megaplots illustrating the steps of the DDA-bif-seaice.
(a) 1298_gt3l_82.637.png – gt3l outer beam, strong [mega 1]
(b) 1298_gt2l_82.727.png – gt2l, center beam, strong [mega 2]
Granule information in caption of Figure 1.

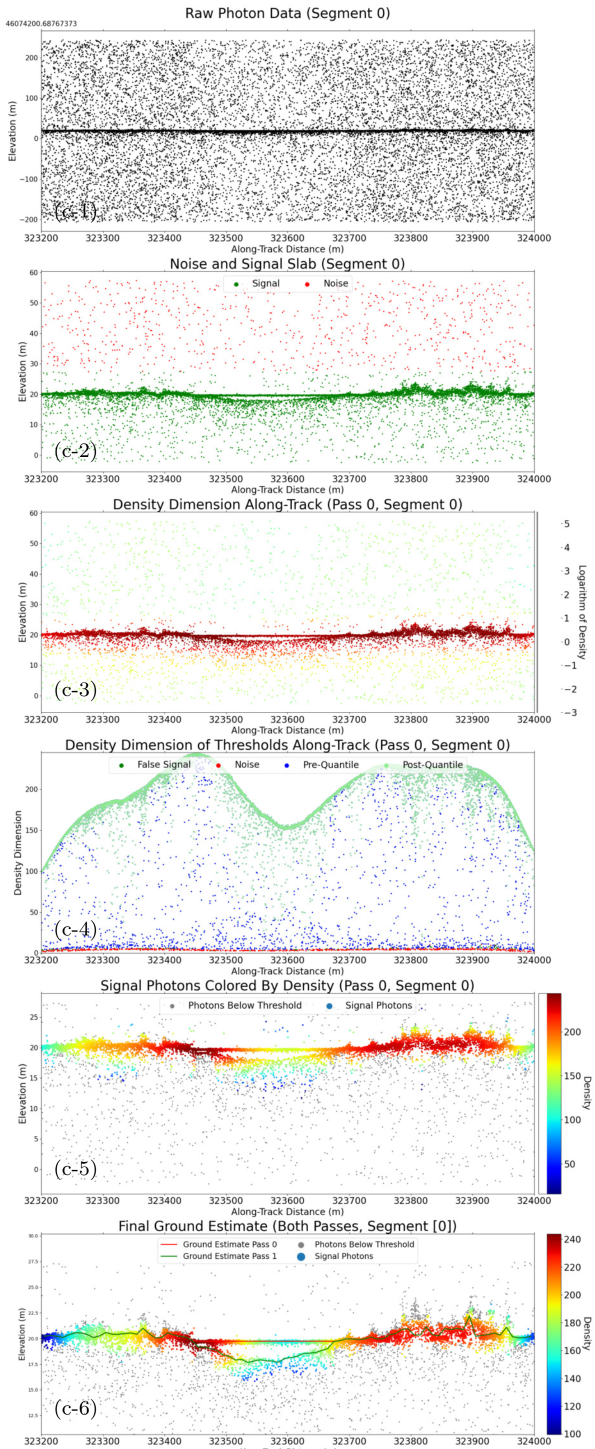

(c) 1237_gt3l_82.818.png [mega 3]

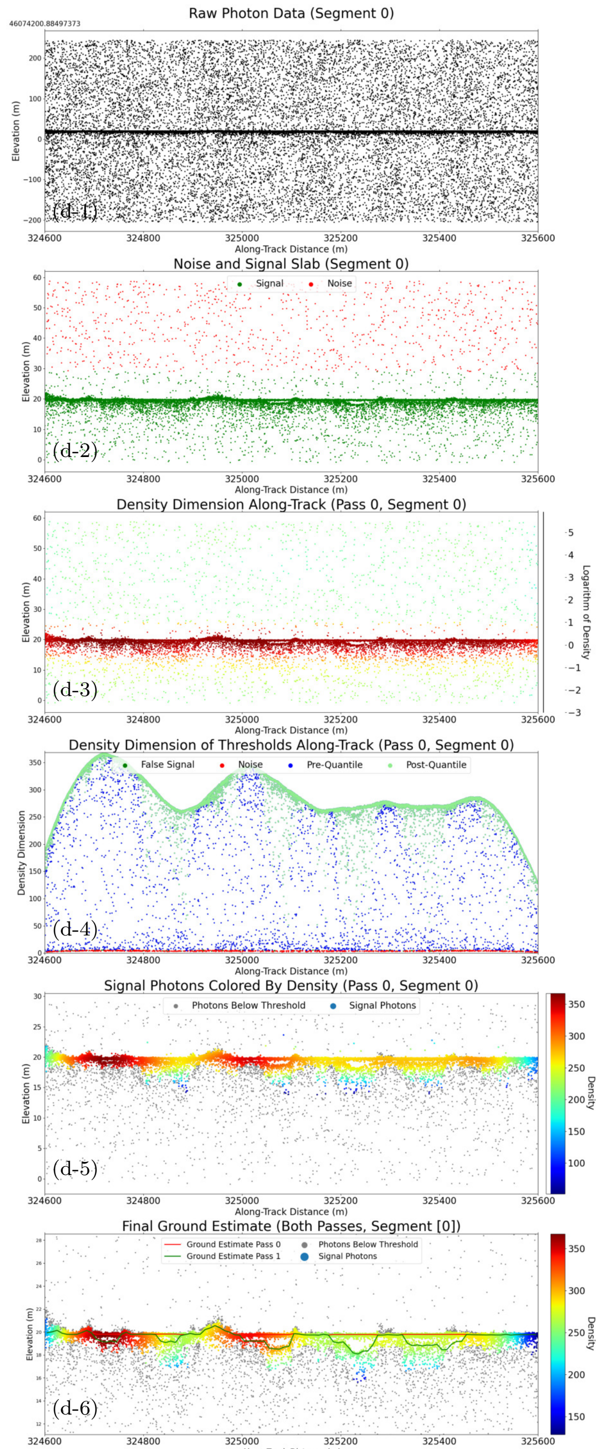

(d) 1237_gt3l_82.831.png [mega 4]

Figure 2, ctd. Megaplots illustrating the steps of the DDA-bif-seaice.
(c) 1237_gt3l_82.818.png – gt3l outer beam, strong [mega 3]; large pond with variable density
(d) 1237_gt3l_82.831.png – gt3l, outer beam, strong [mega 4]
Granule info in caption of Figure 1.

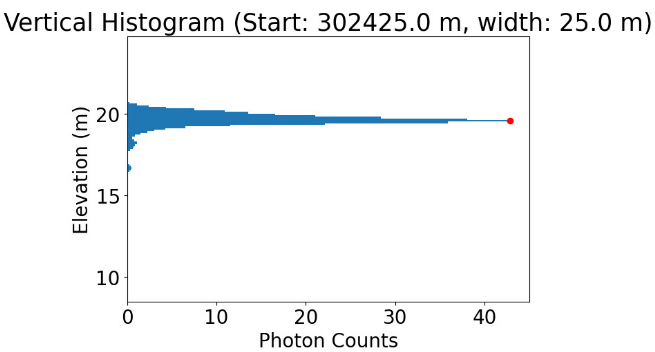

(a) histogram 1

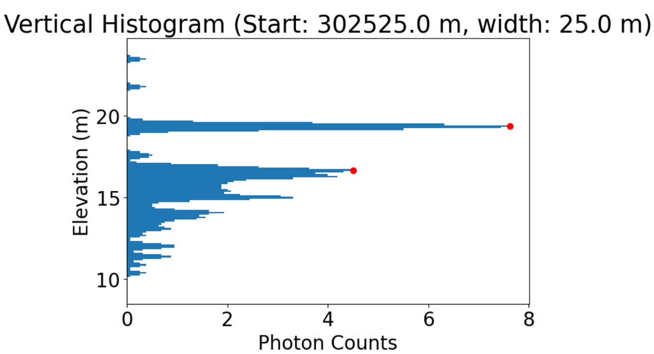

(b) histogram 2

Fig. 3. Histograms illustrating bifurcation criterion in the DDA-bif-seaice submodule ctmp (steps 4.1 and 4.2). (a) Histogram (filtered) typical of a single surface. (b) Histogram (filtered) typical of a melt pond. Histograms stem from example 1298_gt3l_82.637.png, shown in Figure 1e and Figure 2a. – gt3l outer beam, strong. Example from ICESat-2 ATLAS granule ATL03_20190618062235_12370304_005_01.h5, reference ground track (RGT) 1237, collected 2019-June-18, ICESat-2 ASAS version 5 data set.

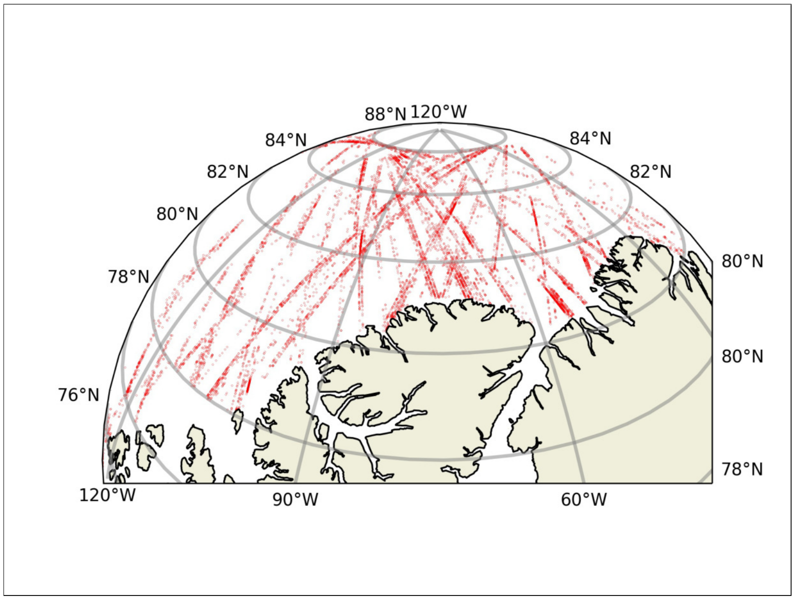

Fig. 4. Location of melt ponds detected by the DDA-bif-seaice in the study area, the multi-year Arctic sea-ice region (MYASIR), for summer 2020. Each small red circle indicates a melt pond detected with the DDA-bif-seaice, a total of approximately 10200 ponds are shown. Note that DDA-bif-seaice was run over about 10% of ICESat-2 tracks, outer strong beams.

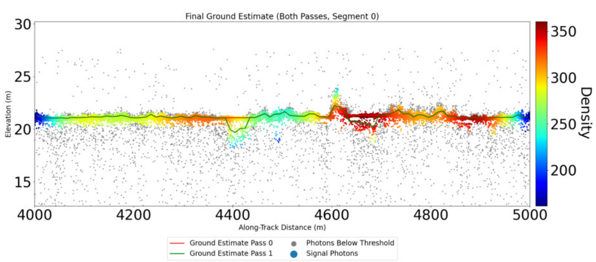

(a) 2019 data, seg0

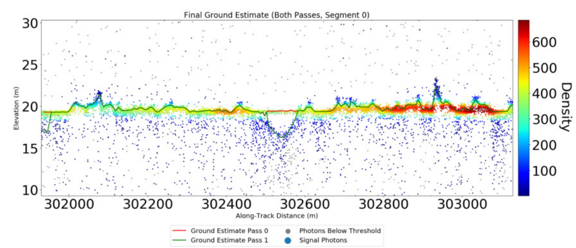

(b) 2020 data, 1298_gt3l_82.637.png

Fig. 5. Automated detection of melt-ponds on sea ice among ridges and complex surfaces with the DDA-bifurcate-seaice. ICESat-2 data from the Lincoln Sea. (a) Example from ICESat-2 ATLAS granule ATL03_20200628121109_00480804_005_01.h5, RGT 48, collected 2020-June-28, ICESat-2 ASAS version 5 data set. Strong outer beam gt1l. Example of two ponds with different different surface heights in complex sea-ice environments. pond 1 (at 4400), pond 2 (at 4600), artifact avoided at 4850. Ground follower not optimized for ridge topography. (b) Application of DDA-bif-seaice (v.16.0) with surface follower for single surfaces optimized to adapt to rough surfaces, such as ridge topography, between ponds. Examples from ICESat-2 ATLAS granule ATL03_20190618062235_12370304_003_01.h5, reference ground track (RGT) 1237, collected 2019-June-18, ICESat-2 ASAS version 3 data set. Same example as Fig. 1e.

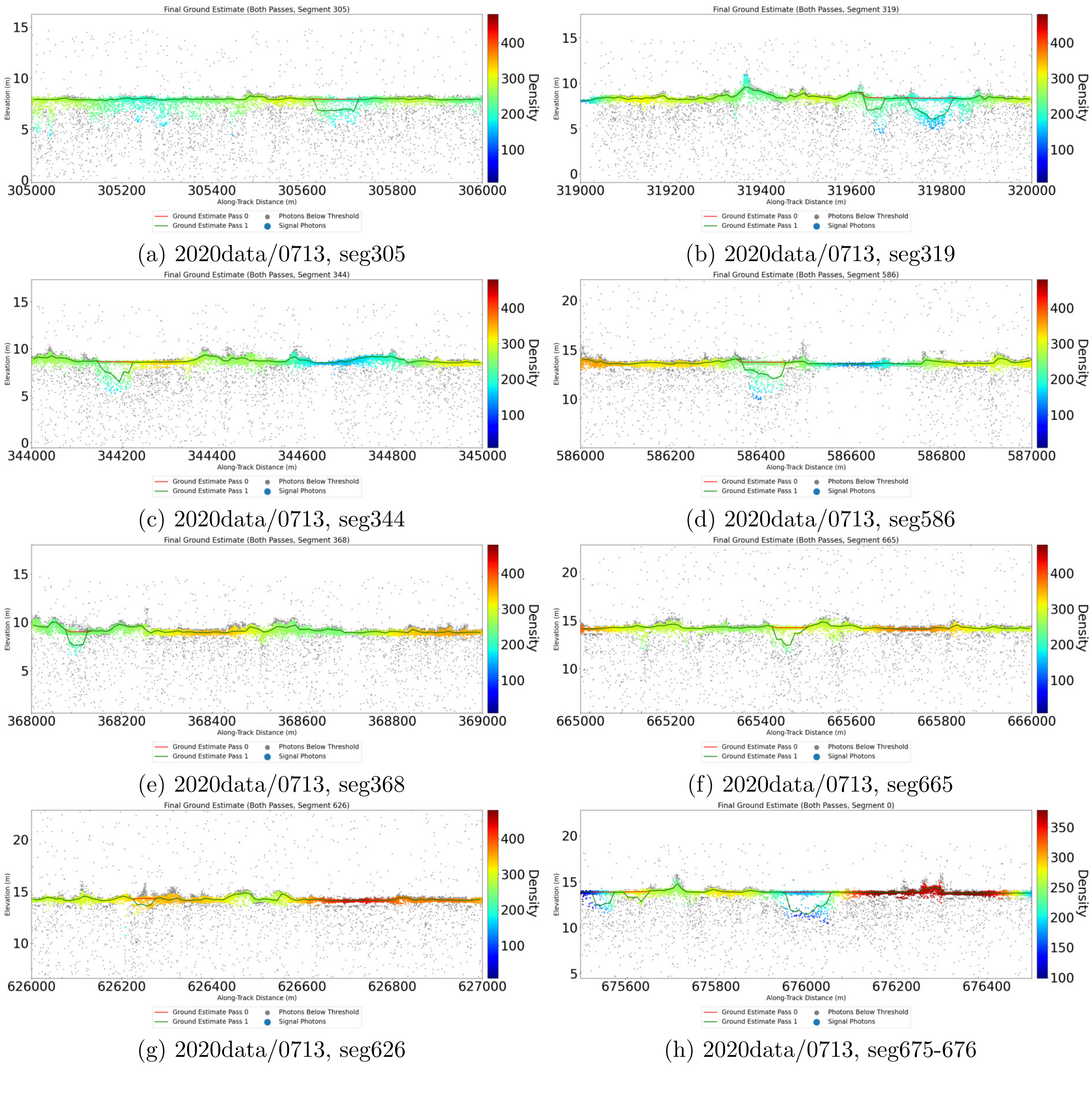

(a) 2020data/0713, seg305

(b) 2020data/0713, seg319

(c) 2020data/0713, seg344

(d) 2020data/0713, seg586

(e) 2020data/0713, seg368

(f) 2020data/0713, seg665

(g) 2020data/0713, seg626

(h) 2020data/0713, seg675-676

Fig. 6. Examples of ponds detected with the DDA-bif-seaice in summer 2020 ICESat-2 ATLAS data, Multi-year Arctic sea-ice region. Examples of ponds are from ICESat-2 ATLAS granule 20200713151204_02790804_005_01 gt1l strong outer beam, reference ground track (RGT) 279, collected 2020-July-13, ICESat-2 ASAS version 5 data set. (a) Pond in the making, located in smooth sea-ice area. Neighboring areas show penetration of ice with water, likely leading up to pond formation. (b) Ponds among ridges area, various formation stages. Surface follower not optimized for ridge topography in the code version. (c) Pond in partly ridged, partly smooth area. (d) Pond in typical location near a ridge. (e) Small pond detected. (f) Small pond detected. no false positive detected in high-density area between 665600 and 665800. (g) DDA avoids dead-time effects (seen as high-density regions below the surface and parallel to the surface. Here, three levels.). Thus DDA avoids false positives. (h) Large pond detected at 676000. Small ponds detected near 675600. Avoidance of saturation effects in regions of high surface reflectance (density 350 or larger).

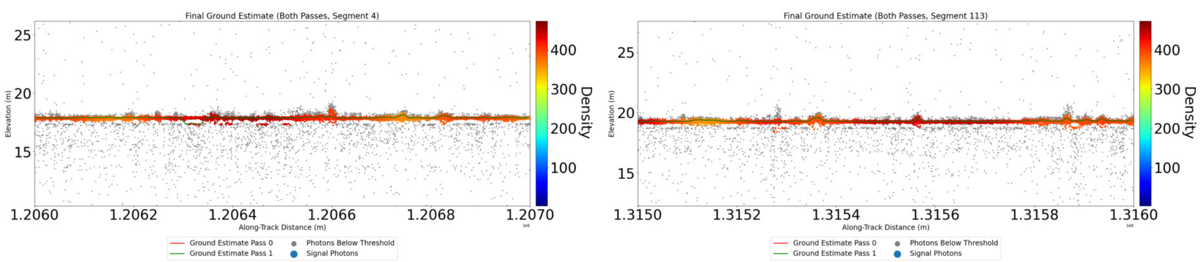

(a) 2020data/0803, seg4

(b) 2020data/0803, seg113

Fig. 7. Avoidance of false positives in DDA-bif-seaice pond detection in highly saturated 2020 ICESat-2 ATLAS sea-ice signals, Multi-year Arctic sea-ice region. Examples of ponds are from ICESat-2 ATLAS granule 20200803013027_05910804_005_01 gt1l strong outer beam, reference ground track (RGT) 591, collected 2020-August-3, ICESat-2 ASAS version 5 data set. (a) A false positive pond identification (between 1.2064 and 1.2066). (b) All false positives are avoided in this segment of dominated by saturated signals.

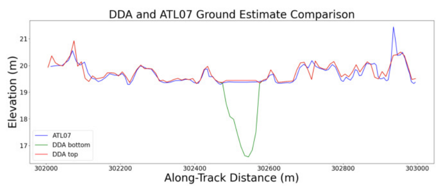

(a) 2019: 1298_gt3l_82.637

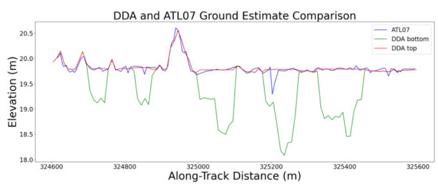

(b) 2019: 1237_gt3l_82.831

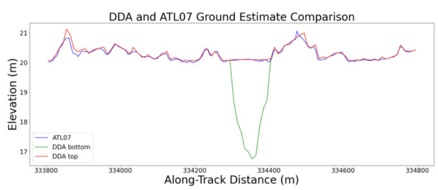

(c) 2019: 1298_gt3l_82.911

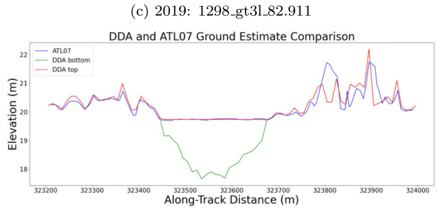

(d) 2019: 1237_gt3l_82.818

(a)

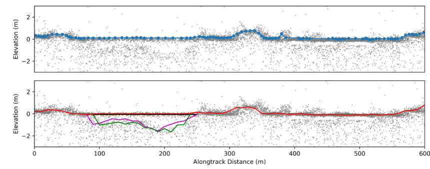

(e) 2020 data: RGT 44 pond

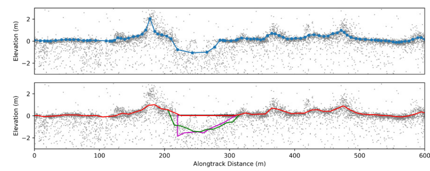

(f) 2020 data: RGT 9 pond

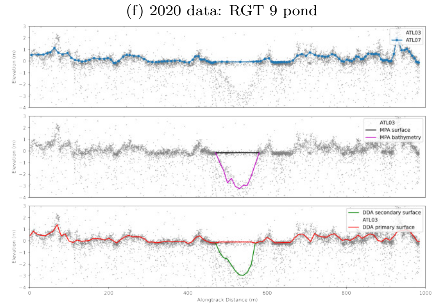

(g) 2019 data: 1298_gt3l_82.637

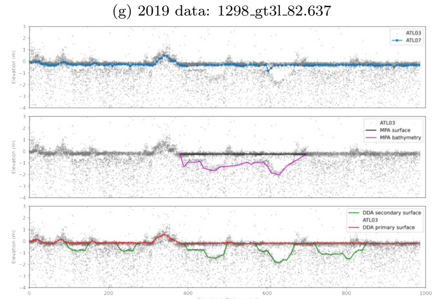

(h) 2019 data: 1237_gt3l_82.831

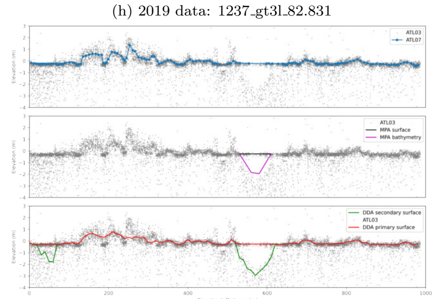

(i) 2010 data: 1298_gt2l_82.727

(b)

Fig. 8. Comparison of pond detection with the DDA-bif-seaice and UMD MPA to results on ICESat-2 ATLAS sea-ice product ATL07. **(8a-8d): Comparison of pond detection with the DDA-bif-seaice to results on ICESat-2 ATLAS sea-ice product ATL07.** Blue- ATL07, red - DDA-bif-seaice surface heights, green – DDA-bif-seaice pond bottom heights. Examples in 8a and 8c are from ICESat-2 ATLAS granule ATL03_20190618062235_12370304_005_01.h5, reference ground track (RGT) 1237, collected 2019-June-18, ICESat-2 ASAS version 5 data set. Examples in 8b and 8d are from ICESat-2 ATLAS granule ATL03_20190622061415_12980304_005_01.h5, RGT 1298, collected 2019-June-22, ICESat-2 ASAS version 5 data set. (a) 2019: 1298_gt3l_82.637 (see Fig. 1e) (b) 2019: 1237_gt3l_82.831 (see Fig. 1d) (c) 2019: 1298_gt3l_82.911 (see Fig 1f) (d) 2019: 1237_gt3l_82.818 (see Fig. 1a) **Comparison of pond detection with the DDA-bif-seaice and the UMD MPA to results reported on ICESat-2 ATLAS sea-ice product ATL07 (8e-8i).** (8e, 8f) 2020 data: Top panels in (a) and (b): ATL07 (blue) . Bottom panels in (a) and (b): green – DDA-bif-seaice pond bottom, magenta – UMD MPA pond bottom, red – DDA-bif-seaice surface of ponds and between ponds. (a, b) from Buckley et al. (in prep). (e) An Example where ATL07 follows the pond surface. Examples in 8e are from ICESat-2 ATLAS granule ATL03_20200628055359_00440804_005_01.h5, RGT 44, strong outer beam gt3l, collected 2020-06-28, ICESat-2 ASAS version 5 data set. start_dt 78559154.55, stop_dt 78559154.71 (f) An Example where ATL07 follows the pond bottom. Examples in 8f are from ICESat-2 ATLAS granule ATL03_20200701061119_00900804_005_01.h5, RGT 90, strong outer beam gt3l, collected 2020-07-01, ICESat-2 ASAS version 5 data set. start_dt 78819350.67, stop_dt 78819350.84 (g, h, i): 2019 data. Examples in 8g and 8i are from ICESat-2 ATLAS granule ATL03_20190622061415_12980304_005_01.h5, RGT 1298, collected 2019-June-22, ICESat-2 ASAS version 5 data set. Examples in 8h are from ICESat-2 ATLAS granule ATL03_20190618062235_12370304_005_01.h5, RGT 1237, collected 2019-June-18, ICESat-2 ASAS version 5 data set. (g) 2019 data: 1298_gt3l_82.637 (see Fig. 1e) (h) 2019: 1237_gt3l_82.831 (see Fig. 1d) (i) 2019: 1298_gt2l_82.727 (see Fig. 1g)

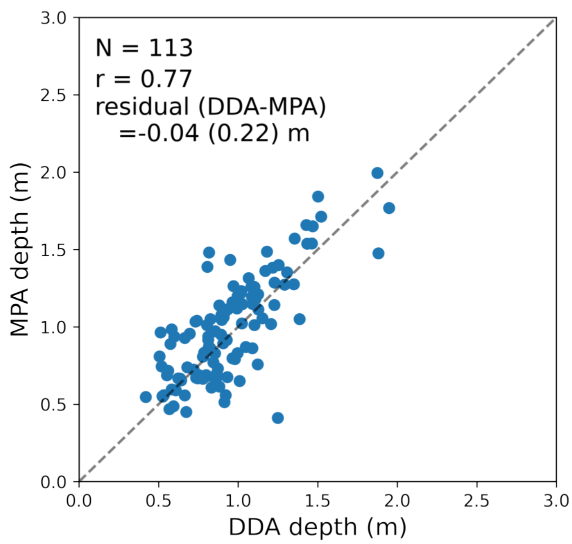

Fig. 9. Scatter plot of mean pond depths for ponds tracked by both the DDA-bif-seaice and the UMD MPA in June and July 2020, 113 ponds total. Residual mean pond depth for DDA-bif-seaice and UMD MPA, calculated as DDA-heights minus MPA-heights.